APL Materials

RESEARCH ARTICLE | OCTOBER 20 2025

Controlling the p-type conductivity of α-SnO thin films by potassium doping

Sieun Chae ; Seungmin Lee ; Anna Park ; M. K. Indika Senevirathna ; Yufan Feng ; Venkanna Kanneboina ; Viet-Anh Ha ; Yaoqiao Hu ; Chaojie Du ; Matthew Barone ; Vladimir Protasenko ; Yilin Evan Li ; Nikolas Podraza ; Kedar Johnson; Debdeep Jena ; Huili G. Xing ; Xiaoqing Pan ; Kyeongjae Cho ; Feliciano Giustino ; Michael D. Williams ; Darrell G. Schlom

APL Mater. 13, 101114 (2025)
https://doi.org/10.1063/5.0288742
CHORUS

AIP Publishing

Controlling the p-type conductivity of α-SnO thin films by potassium doping

Cite as: APL Mater. 13, 101114 (2025); doi: 10.1063/5.0288742
Submitted: 2 July 2025 • Accepted: 22 September 2025 •
Published Online: 20 October 2025

Sieun Chae,[1] Seungmin Lee,[1] Anna Park,[1] M. K. Indika Senevirathna,[2] Yufan Feng,[3] Venkanna Kanneboina,[4,5] Viet-Anh Ha,[6,7] Yaoqiao Hu,[8] Chaojie Du,[9] Matthew Barone,[10] Vladimir Protasenko,[11] Yilin Evan Li,[1] Nikolas Podraza,[4,5] Kedar Johnson,[2] Debdeep Jena,[1,11,12] Huili G. Xing,[1,11,12] Xiaoqing Pan,[9] Kyeongjae Cho,[8] Feliciano Giustino,[6] Michael D. Williams,[2] and Darrell G. Schlom[1,12,13,a)]

AFFILIATIONS

[1]Department of Materials Science and Engineering, Cornell University, Ithaca, New York 14853, USA
[2]Department of Physics, Clark Atlanta University, Atlanta, Georgia 30314, USA
[3]Robert Frederick Smith School of Chemical and Biomolecular Engineering, Cornell University, Ithaca, New York 14853, USA
[4]Department of Physics and Astronomy, The University of Toledo, Toledo, Ohio 43606, USA
[5]Wright Center for Photovoltaics Innovation and Commercialization, The University of Toledo, Toledo, Ohio 43606, USA
[6]Oden Institute for Computational Engineering and Sciences, The University of Texas at Austin, Austin, Texas 78712, USA
[7]Department of Physics, The University of Texas at Austin, Austin, Texas 78712, USA
[8]Department of Materials Science and Engineering, University of Texas at Dallas, Dallas, Texas 75080, USA
[9]Department of Materials Science and Engineering, University of California at Irvine, Irvine, California 92697, USA
[10]Platform for the Accelerated Realization, Analysis, and Discovery of Interface Materials (PARADIM), Cornell University, Ithaca, New York 14853, USA
[11]School of Electrical and Computer Engineering, Cornell University, Ithaca, New York 14853, USA
[12]Kavli Institute at Cornell for Nanoscale Science, Ithaca, New York 14853, USA
[13]Leibniz-Institut für Kristallzüchtung, 12489 Berlin, Germany

[a)]**Author to whom correspondence should be addressed:** schlom@cornell.edu

ABSTRACT

Development of a high-performance, p-type oxide channel is crucial to realize all-oxide complementary metal–oxide semiconductor technology that is amenable to 3D integration. Among p-type oxides, α-SnO is one of the most promising owing to its relatively high hole mobility {as high as 21 $cm^2\ V^{-1}\ s^{-1}$ has been reported [M. Minohara *et al.*, J. Phys. Chem. C **124**, 1755–1760 (2020)]}, back-end-of-line compatible processing temperature (≤400 °C), and good optical transparency for visible light. Unfortunately, doping control has only been demonstrated over a limited range of hole concentrations in such films. Here, we demonstrate systematic control of the hole concentration of α-SnO thin films via potassium doping. First-principles calculations identify potassium substitution on the tin site (K_{Sn}) of α-SnO to be a promising acceptor that is not (self)-compensated by native vacancies or potassium interstitials (K_i). We synthesize epitaxial K-doped α-SnO thin films with controlled doping concentration using suboxide molecular-beam epitaxy. The concentration of potassium is measured by secondary ion mass spectrometry, and its incorporation into the α-SnO structure is corroborated by x-ray diffraction. The effect of potassium doping on the optical response of α-SnO is measured by spectroscopic ellipsometry. Potassium doping provides systematic control of hole doping in α-SnO thin films over the 4.8×10^{17} to 1.5×10^{19} cm^{-3} range without significant degradation of hole mobility or the introduction of states that absorb visible light. Temperature-dependent Hall measurements reveal that the potassium is a shallow acceptor in α-SnO with an ionization energy in the 10–20 meV range.

INTRODUCTION

Oxide-based thin-film transistors (TFTs) have great potential in transparent electronic applications. While n-type oxide semiconductors have already been extensively applied in flat-panel displays and flexible electronics,[1,2] the development of p-type oxides is crucial to enable complementary metal–oxide semiconductor (CMOS), a key component of energy-efficient integrated circuits. Back-end-of-line compatible p-channel field-effect transistors have been identified as a key ingredient for disruptive scaling of devices by vertical integration.[3–5] The potential for power savings is similar to the 100–1000 times less power used by CMOS compared with the n-type metal–oxide semiconductor (NMOS) in silicon transistor technology.[3,6] Owing to the localized nature of O 2*p* orbitals, p-type oxides must employ hybridization of the O 2*p* orbitals with filled cation *s*-/*d*-orbitals (such as Sn^{2+}, Bi^{3+}, and Cu^{+}) to form dispersive valence bands.[7–9] Among such candidates, α-SnO is one of the most promising p-type materials relevant to industrial applications due to its relatively high hole mobility, good optical transparency in the visible light region, and back-end-of-line (BEOL) compatible processing temperature. A record Hall mobility of 21 $cm^2\ V^{-1}\ s^{-1}$ has been demonstrated for α-SnO films synthesized by pulsed-laser deposition on yttria stabilized zirconia (YSZ) substrates,[10] and a field-effect mobility up to 7.6 $cm^2\ V^{-1}\ s^{-1}$ has been reported for sputtered SnO TFTs with HfO_2 gate dielectrics.[11] The p-type nature of undoped SnO films is attributed to native defects, such as Sn vacancies (V_{Sn}) or unintentional incorporation of hydrogen.[12,13] Although a relatively high mobility has been achieved in undoped SnO films, the range of hole carrier control achieved was only (0.5–1) × 10^{17} cm^{-3},[10] which is insufficient for most devices. To improve the electrical properties for technical adoption, better control of the carrier concentration through extrinsic doping, in contrast to intrinsic native defects, is needed.

Recent advances in theoretical methodologies and computational power have allowed an extensive search for useful dopant elements in α-SnO.[14] Among the identified dopants, experimental studies have focused on Na^{+}, K^{+}, Ga^{3+}, Y^{3+}, Sb^{3+}, and La^{3+}.[15–21] Though Hosono *et al.*[16] established that Sb^{3+} was an n-type dopant in SnO as expected for the substitution of a cation with higher valence onto the Sn^{2+}-site of SnO, La^{3+}, Y^{3+}, and Ga^{3+} doping have been reported to enhance the p-type conductivity.[16–19] Meanwhile doping with K^{+} has been reported to suppresses the hole concentration,[19] while doping with Na^{+} increases the hole concentration as expected for the substitution of a cation with lower valence onto the Sn^{2+}-site of SnO.[20] Such inconsistencies between theory and experiment highlight the challenges of producing doped SnO thin films with controlled carrier concentration, i.e., controlling dopants to occupy desired substitutional sites or suppressing charge compensation from the interplay between charged defects.

Motivated by the calculations of Graužinytė *et al.*[14] showing that potassium is likely to be the best p-type dopant for α-SnO, we use a deposition method with a simpler reaction pathway than has been used before for K-doped α-SnO films to see if the predicted benefits of potassium as a dopant can be realized. These predicted benefits include (1) the second-lowest formation energy of all dopants for substitution onto the Sn^{2+}-site of α-SnO (K_{Sn}), (2) an ionization energy calculated to be <100 meV, and (3) in contrast to the dopant with lowest formation energy, sodium, substitution of potassium is predicted to not give rise to any defect states in SnO that would absorb visible light.[14] This means that potassium should be a p-type dopant that does not degrade the optical transparency of α-SnO films.

Prior studies of potassium doping in SnO films utilized solely solution-based processing methods.[19,22] In the first study, the high potassium doping (5%–30%) studied led to all of the K-doped films showing two crystalline phases in x-ray diffraction (XRD): α-SnO_2 and what was tentatively identified as $K_2Sn_2O_3$.[22] In the second study, potassium doping was found to result in the formation of the metastable orthorhombic polymorph of β-SnO (also known as red SnO), so rather than studying K-doped α-SnO (also known as black SnO), what was studied was K-doped β-SnO.[19]

In this paper, we demonstrate systematic modulation of the carrier concentration in K-doped α-SnO thin films grown by suboxide molecular-beam epitaxy (S-MBE). We synthesized K-doped SnO thin films under BEOL-compatible conditions (at a substrate temperature of <375 °C) utilizing a molecular beam of the suboxide SnO. Our films remain single-phase and epitaxial with the addition of potassium dopants, where the concentration of dopants is measured by secondary ion mass spectroscopy (SIMS). The p-type conductivity is successfully controlled by potassium doping; potassium enhances the hole density by nearly two orders of magnitude, while impurity scattering leads to a relatively small decrease in the hole mobility. This agrees with our first-principles calculations that potassium dopants prefer (1) to substitute on the Sn^{2+}-site of α-SnO, providing holes not compensated by native defects, and (2) the calculated mobility decreases with increasing hole density due to ionized impurity scattering. The optical bandgap measured by spectroscopic ellipsometry remains nearly constant as the potassium concentration is varied showing that no highly absorbing defect level is induced in the midgap. Our results suggest that potassium effectively substitutes on the tin site and provide holes that can enhance the p-type conductivity by ~25 times.

METHODS

Band structure and defect calculations

First-principles calculations were based on hybrid density functional theory (DFT) using the projector augmented wave (PAW) method and the Heyd–Scuseria–Ernzerhof (HSE06) functional as implemented in the Vienna *ab initio* Simulation Package (VASP).[23] In all calculations, the Perdew–Burke–Ernzerhof (PBE) pseudopotentials[24] and a plane wave energy cutoff of 500 eV were employed with Sn $5s^2 5p^2$, O $2s^2 2p^4$, and K $3p^6 4s^1$ treated as valence electrons. The band structure of the bulk α-SnO was calculated with a fully relaxed primitive cell and a Γ-centered 4 × 4 × 3 Brillouin zone sampling grid. We used the standard mixing parameter of 25% in HSE06,[25] which produces an indirect bandgap (E_g) of 0.75 eV and lattice parameters of a = 3.793 Å and c = 5.005 Å. The calculated bandgap and lattice parameters show good agreement with the experimental values (E_g = 0.7 eV, a = 3.801 Å, and c = 4.835 Å),[26,27] albeit ~3% overestimation of the interlayer distance.

Defect calculations were performed with 3 × 3 × 2 supercells (i.e., 72 atoms) and a Γ-centered 2 × 2 × 2 Brillouin zone sampling grid. All defect structures were relaxed with HSE06 until the forces on the ions were less than 0.02 eV/Å. Spin polarized calculations

were performed for defect structures with unpaired electrons. The formation energy of a point defect is determined by the scheme of Freysoldt *et al.*[28] The correction energy for the unphysical electrostatic interaction between periodic charged defects was calculated with the SXDEFECTALIGN code,[29] and the static dielectric constant of 17.7 was used.[14] The limits on chemical potentials were bounded by the stability condition of the solid, i.e., $\mu_{Sn} + \mu_O = \Delta H^f(SnO)$, and set to the oxygen-poor limit to simulate our experimental synthesis condition. Formation of the K_4SnO_4 secondary phase was considered to calculate $\Delta\mu_K$. The calculated values for $\Delta H^f(SnO)$ and $\Delta H^f(K_4SnO_4)$ are −2.556 and −13.998 eV, respectively. For the potassium defect substituting on the tin site (K_{Sn}), the formation of hole polarons is considered by distorting the defect site and relaxing the structure by breaking the symmetry. The calculated polaronic state is 1 meV higher in energy compared to the undistorted structure, indicating that the formation of a polaron is not likely.

Mobility calculation

- **Drude's model**
  We calculate mobility considering various scattering mechanisms. Phonon-limited mobility in a perfect single crystal of α-SnO is predicted in our previous work.[30] In this paper, we investigate how charged impurities influence the mobilities as a function of defect concentration. Ionized impurity scattering modeling was based on the Conwell–Weisskopf approach,[31] in which the electron relaxation time is given by[32]

$$\tau(E) = \frac{16\sqrt{2m^*}\varepsilon^2}{N_{II}q^4}\left[\ln\left(1+\gamma^2\right) - \frac{\gamma^2}{1+\gamma^2}\right]E^{\frac{3}{2}}, \quad (1)$$

  where E is the energy of electron hole, m^* is the effective mass, ε is the dielectric constant, N_{II} is the concentration of ionized impurity charge, q is the elementary charge, $\gamma^2 = 8m^*EL_D^2/\hbar^2$, and L_D is the Debye length. Electron mobility is then calculated based on the Drude model, $\mu = \frac{q\langle\tau\rangle}{m^*}$, where $\langle\tau\rangle$ is the average relaxation time considering all electronic states at different energy states E, $\langle\tau\rangle = \int D(E)f(E)\tau(E)dE$, where $D(E)$ is the density of states and $f(E)$ is the Fermi–Dirac function.[30]
- ***Ab initio* Boltzmann transport equation**
  The fully detailed derivation of the *ab initio* Boltzmann transport equation (*ai*BTE) formalism can be found in Refs. 33 and 34. Here, we briefly rewrite the theory and computational steps implemented in this work. The carrier mobility tensor, in the weak electric field limit, is calculated as

$$\mu_{\alpha\beta} = \frac{1}{n_c\Omega}\frac{1}{N_{\boldsymbol{k}}}\sum_{n\boldsymbol{k}} v_{n\boldsymbol{k},\alpha}\partial_{E_\beta}f_{n\boldsymbol{k}}, \quad (2)$$

  where the Greek indices indicate Cartesian directions, n_c is the carrier density, Ω is the volume of the crystal unit cell, $N_{\boldsymbol{k}}$ is the number of electron wavevectors $\boldsymbol{k}$ in a uniform Brillouin zone grid, $v_{n\boldsymbol{k},\alpha}$ denotes the electron group velocity along the Cartesian direction α for the electronic state with band n and wavevector $\boldsymbol{k}$, and $\partial_{E_\beta}f_{n\boldsymbol{k}}$ is the derivative of the carrier occupation function with respect to the β-component of the electric field, evaluated at vanishing field. The variation $\partial_{E_\beta}f_{n\boldsymbol{k}}$ is obtained from the self-consistent solution of the *ai*BTE,

$$-ev_{n\boldsymbol{k}}^{\beta}\frac{\partial f_{n\boldsymbol{k}}^0}{\partial\varepsilon_{n\boldsymbol{k}}} = \frac{1}{N_{\boldsymbol{q}}}\sum_{m\boldsymbol{q}}\left(\Gamma_{m\boldsymbol{k}+\boldsymbol{q}\to n\boldsymbol{k}}\partial_{E_\beta}f_{m\boldsymbol{k}+\boldsymbol{q}} - \Gamma_{n\boldsymbol{k}\to m\boldsymbol{k}+\boldsymbol{q}}\partial_{E_\beta}f_{n\boldsymbol{k}}\right), \quad (3)$$

  where e is the electron charge, $f_{n\boldsymbol{k}}^0$ denotes the Fermi–Dirac occupation of the state $n\mathbf{k}$, $N_{\boldsymbol{q}}$ is the number of phonon wavevectors $\mathbf{q}$ in the Brillouin zone grid, and $\Gamma_{n\boldsymbol{k}\to m\boldsymbol{k}+\boldsymbol{q}}$ denotes the scattering rate from the state $n\mathbf{k}$ to the state $m\mathbf{k}+\mathbf{q}$.

The electron–phonon scattering rate is written as

$$\Gamma_{n\boldsymbol{k}\to m\boldsymbol{k}+\boldsymbol{q}}^{(ph)} = \sum_v \frac{2\pi}{\hbar}\left|g_{mnv}(\boldsymbol{k},\boldsymbol{q})\right|^2 \times \left[\left(n_{\boldsymbol{q}v}+1-f_{m\boldsymbol{k}+\boldsymbol{q}}^0\right)\delta\left(\varepsilon_{n\boldsymbol{k}}-\varepsilon_{m\boldsymbol{k}+\boldsymbol{q}}-\hbar w_{\boldsymbol{q}v}\right) + \left(n_{\boldsymbol{q}v}+f_{m\boldsymbol{k}+\boldsymbol{q}}^0\right)\delta\left(\varepsilon_{n\boldsymbol{k}}-\varepsilon_{m\boldsymbol{k}+\boldsymbol{q}}+\hbar w_{\boldsymbol{q}v}\right)\right], \quad (4)$$

where $\hbar$ is the reduced Planck constant, $g_{mnv}(\boldsymbol{k},\boldsymbol{q})$ is the electron–phonon (el–ph) matrix element for the scattering between Kohn–Sham states $n\mathbf{k}$ and $m\mathbf{k}+\mathbf{q}$ via the phonon of wavevector $\mathbf{q}$ in branch v,[35] $n_{\boldsymbol{q}v}$ denotes the Bose–Einstein occupation of this mode, $w_{\boldsymbol{q}v}$ is the corresponding vibrational frequency, and $\varepsilon_{n\boldsymbol{k}}$ and $\varepsilon_{m\boldsymbol{k}+\boldsymbol{q}}$ denote the band eigenvalues obtained from the mean-field DFT or many-body method within the GW approximation. The electronic band structure, phonon band structure, and el–ph matrix elements are interpolated from coarse to very dense grid in the Brillouin zone employing the Wannier–Fourier interpolation technique.[36]

The interpolation of $g_{mnv}(\boldsymbol{k},\boldsymbol{q})$ needs to be implemented with caution for polar materials, in which the long-range dipole electric field induced by LO phonon creates divergence at long wavelength.[37,38] Moreover, we also considered the impact of a dynamical quadrupole[39,40] relating to piezoelectric effects.[41]

For ionized impurities, we developed an *ab initio* method to calculate the ionized-impurity scattering rate as in Ref. 42,

$$\Gamma_{n\boldsymbol{k}\to m\boldsymbol{k}+\boldsymbol{q}}^{(ii)} = n_{imp}\frac{2\pi e^4Z^2}{\hbar\epsilon_0^2\Omega}\sum_{\boldsymbol{G}\neq-\boldsymbol{q}}\frac{\left|\left\langle u_{m\boldsymbol{k}+\boldsymbol{q}}\left|e^{i\boldsymbol{G}\cdot\boldsymbol{r}}\right|u_{n\boldsymbol{k}}\right\rangle\right|^2}{\left|(\boldsymbol{q}+\boldsymbol{G})\cdot\boldsymbol{\epsilon}^0\cdot(\boldsymbol{q}+\boldsymbol{G})\right|^2}\delta\left(\varepsilon_{n\boldsymbol{k}}-\varepsilon_{m\boldsymbol{k}+\boldsymbol{q}}\right), \quad (5)$$

where n_{imp} is the impurity concentration, ϵ_0 and ϵ^0 are the vacuum permittivity and the electronic dielectric permittivity tensor, respectively. $\boldsymbol{G}$ denotes the reciprocal lattice vectors, and $u_{n\boldsymbol{k}}$ is the lattice-periodic part of the Kohn–Sham state. We note that

Eq. (5) was formulated via the Kohn–Luttinger ensemble average procedure.[43]

The grain boundary scattering is also treated via simple model. Given the carrier velocity $v_{n\mathbf{k}}$, the scattering rate in this model is $\Gamma^{(ed)}_{n\mathbf{k}} = |v_{n\mathbf{k}}|/L$, where L is the grain size. This model has been widely used for thermal transport.[43–46] The grain size L is set as an external parameter.

The DFT calculations are performed using the PWscf code in the Quantum ESPRESSO suite.[47,48] We employ the PBE exchange-correlation functional.[24] Structural optimization is obtained with the **k**-mesh of 10 × 10 × 8, criteria for force <2.5 × 10^{-4} eV/Å, pressure <0.05 kbar, and total energy <1.5 × 10^{-5} eV. We utilize optimized norm-conserving pseudopotentials[49] from the PseudoDojo library[50] with a plane wave kinetic energy cutoff of 96 Ry as recommended. The phonon calculations are performed on a coarse **q**-mesh of 5 × 5 × 4 within the Density Functional Perturbation Theory (DFPT) using the PHonon code in Quantum ESPRESSO suite.[47,48] We note that the spin–orbit effect does not modify the electronic structure of α-SnO, thus it was neglected in our calculations. The quasiparticle *GW* calculations are implemented using the BerkeleyGW code.[51,52] We employ a dielectric matrix kinetic energy cutoff of 25 Ry, 420 empty bands for the summation over states, and the Hybertsen–Louie plasmon-pole model. The *GW* band structures are used to obtain more accurate band curvature (see Fig. S1), which are then used to solve the *ai*BTE Eq. (3). The quadrupole tensor is calculated using the method in Ref. 53 via the ABINIT code (see Table S1).[53] The electronic band structure, phonon band structure, and el–ph matrix element are interpolated on very dense wavevector grids of 90 × 90 × 72 for both holes and phonons in the EPW code.[36] The charge state of ionized impurities is $Z = -1$, representing the fact that K_{Sn} acceptors are used in our experiments; the ionized-impurity density is $n_{imp} = n_c$. The grain size L is chosen between 100 and 200 nm as observed in the AFM image (see Fig. S2). The *ai*BTE is solved self-consistently using the EPW code.[36]

Thin film synthesis

Thin films of K-doped α-SnO are synthesized on the (001)-oriented yttria-stabilized cubic zirconia (YSZ) substrates containing 9.5 mol. % Y_2O_3 by *S*-MBE. The SnO_2 powder (Alfa Aesar, 99.996%) is used as the source material to create a pre-oxidized molecular beam of SnO. SnO is an ideal molecular beam from which α-SnO films can be grown because the molecular species arrive to the substrate pre-oxidized in the desired Sn^{2+} oxidation state.[54,55] The thermodynamic calculations of the vapor pressure of SnO emanating from SnO_2 indicate that at typical *S*-MBE growth rates, the vapor pressure of SnO is over four orders of magnitude higher than any other species, meaning that the SnO molecular beam is more than 99.99% SnO.[54,56,57] The dominance of the SnO (g) in the molecular beam emitted by a crucible containing SnO_2 (s) has been observed experimentally using mass spectrometry, where the gas and solid phases are denoted by (g) and (s), respectively.[58] We refer to this approach of growing epitaxial films from suboxide molecular beams as suboxide MBE.[56,59,60] Using *S*-MBE, the difficulty of trying to oxidize a tin molecular beam with just the right amount of oxygen, oxygen plasma, NO_2, or ozone to achieve Sn^{2+}—the traditional MBE approach that has never succeeded in producing phase-pure SnO[61–63]—is overcome. The flux of SnO is varied from 2 × 10^{12} to 7 × 10^{13} molecules/(cm^2 s) [as measured by a quartz crystal microbalance (QCM)] to measure the effect of the SnO flux on film roughness. The background pressure during growth ranges from 1 × 10^{-7} to 7 × 10^{-7} Torr depending on the SnO flux. The background pressure includes all species emitted from the SnO_2 (s) source and no additional oxygen-containing species (i.e., no additional O_2, O_3, or plasma) are supplied. Prior to film deposition, the YSZ substrates are laser-annealed at 1200 °C for 200 s in ozone (~10% O_3 + 90% O_2).[64] The films are all grown at substrate temperatures ranging from 285 to 375 °C and consist of a 10 nm thick unintentionally doped α-SnO buffer layer followed by a 50 nm thick K-doped α-SnO layer. The samples are labeled by A#, where # = 1, 2, . . ., 21. The substrate temperature and the potassium effusion cell temperature for each sample are indicated in Table S2. After finishing deposition, the films are cooled with the shutter of the potassium effusion cell open to minimize the loss of potassium from the sample. The potassium dopant is supplied from an effusion cell containing an In_4K intermetallic compound prepared in a nitrogen-filled glovebox before loading (in air) into the MBE system.[65] The concentration of potassium in the films is controlled by varying the temperature of the effusion cell from 25 to 260 °C. X-ray diffraction (XRD) is measured using a Malvern Panalytical Empyrean four-circle diffractometer with a 1.5406 Å Cu $K\alpha_1$ source. The Hall effect measurements are performed in a van der Pauw geometry at room temperature on the 10 × 10 mm^2 samples with indium contacts deposited on the corners.[66]

Spectroscopic ellipsometry

Ellipsometric spectra in terms of $N = \cos 2\psi$, $C = \sin 2\psi \cos \Delta$, and $S = \sin 2\psi \sin \Delta$ are collected for epitaxial SnO films over a photon energy range of 0.73–5.87 eV at 50°–70° angles of incidence in 5° intervals using a single rotating compensator multichannel ellipsometer[67,68] (J.A. Woollam Co., M-2000FI), where $\tan\psi$ and Δ are the amplitude ratio and phase difference between the electric field components polarized parallel and perpendicular to the plane of incidence, respectively. Data analysis is performed using the CompleteEASE software (J.A. Woollam Co.). The complex dielectric function ($\varepsilon = \varepsilon_1 + i\varepsilon_2$) spectra and the structural parameters are determined using the divided spectral range analysis.[69–73] The structural model includes a semi-infinite YSZ substrate, interface, epitaxially grown thin film, and a surface layer. The reference spectra in ε of the YSZ substrate have been previously obtained.[74] Spectra in ε of the surface layer are represented using a Bruggeman effective medium approximation consisting of 0.5 void and 0.5 bulk film volume fractions.[75] Spectra in ε of the interface layer are also represented by a Bruggeman effective medium approximation consisting of variable fractions of void and epitaxial film; this layer represents a lower optically dense material near the substrate/epitaxial film interface.

In divided spectral range analysis, the ellipsometric spectra are divided into photon energy ranges from 0.73 to 2.3 eV and 2.9–5.87 eV corresponding to spectral regions, where these thin films are optically transparent and heavily absorbing, respectively. Spectra in ε in the transparent region are fitted with a Sellmeier expression[76] and a constant additive (ε_∞) term to ε_1 fixed at 1. In the highly absorbing region above the bandgap, spectra in ε are represented by the critical point parabolic band (CPPB) oscillators, a

Sellmeier expression, and $\varepsilon_\infty = 1$.[77] Both transparent and highly absorbing spectral regions are fitted simultaneously by using the respective parametric model to describe ε in that spectral region with common structural parameters, which include the bulk film, surface layer, and interface layer thicknesses and the relative void fraction in the interface layer. Numerical inversion[78] is then performed using the structural parameters from the divided spectral range analysis to obtain ε over the full measured spectral range for all samples.

RESULTS

We first predict the band structure, p-type dopability with potassium doping, and doping concentration-dependent hole mobility of α-SnO using the first-principles calculations. Figures 1(a) and 1(b) compare the HSE06-calculated band structures and wavefunctions of SnO_2 and α-SnO, respectively. While the valence band maximum (VBM) of SnO_2 is composed of the localized O 2*p* orbitals as represented in the inset figure, the VBM of α-SnO is composed of the hybridization between O 2*p* and Sn 5*s* orbitals, resulting in a highly dispersive VBM. Figure 1(c) shows the formation energy of potassium defects in potential defect sites along with the native point defects as a function of the Fermi energy. For native point defects, we considered tin and oxygen vacancies (V_{Sn} and V_O) as they have been reported to be the dominant native defects of α-SnO that are electrically active in previous studies.[12,14] In addition, we assumed that the commonly present impurities, such as hydrogen or nitrogen, are not likely to incorporate in our experimental conditions as the base vacuum of our growth chamber remains relatively low ($<8 \times 10^{-8}$ Torr) and the growth of α-SnO thin films results from a condensation of SnO (g) from a molecular beam without any additional gas supply. We predict V_{Sn} is an acceptor-type defect with an acceptor ionization energy of 72 meV, while V_O is a deep donor defect with a donor ionization energy of 0.395 eV. These results agree well with the previous report by Varley *et al.*[12] In the absence of extrinsic dopants, the Fermi energy is pinned at merely 0.234 eV above the valence bands, suggesting the intrinsic p-type nature of α-SnO.

We next calculate the formation energy of potassium defects in possible defect sites, i.e., potassium substitution for tin (K_{Sn}), potassium substitution for oxygen (K_O), and interstitial potassium (K_i), as illustrated in Fig. 1(c). For K_i, we calculate two potential interstitial sites between the interlayers and plot the one with the lowest formation energy. We predict K_{Sn} is an acceptor with an ionization energy of 86 meV and has the lowest formation energy over the entire Fermi energy range among the possible defects we studied (including native defects). The predicted ionization energy value is very close to that of K_{Sn} reported by Ref. 14 (between 49 and 93 meV). Any difference might arise from the fact that Ref. 14 used a larger supercell containing 192 atoms and the structure is relaxed using a PBE functional. Our study suggests that K_{Sn} is an excellent acceptor dopant that is not likely to be compensated by native defects. Assuming $T_{sub} = 375\,^\circ$C (the deposition temperature in our experiment), we used an Arrhenius equation to calculate the

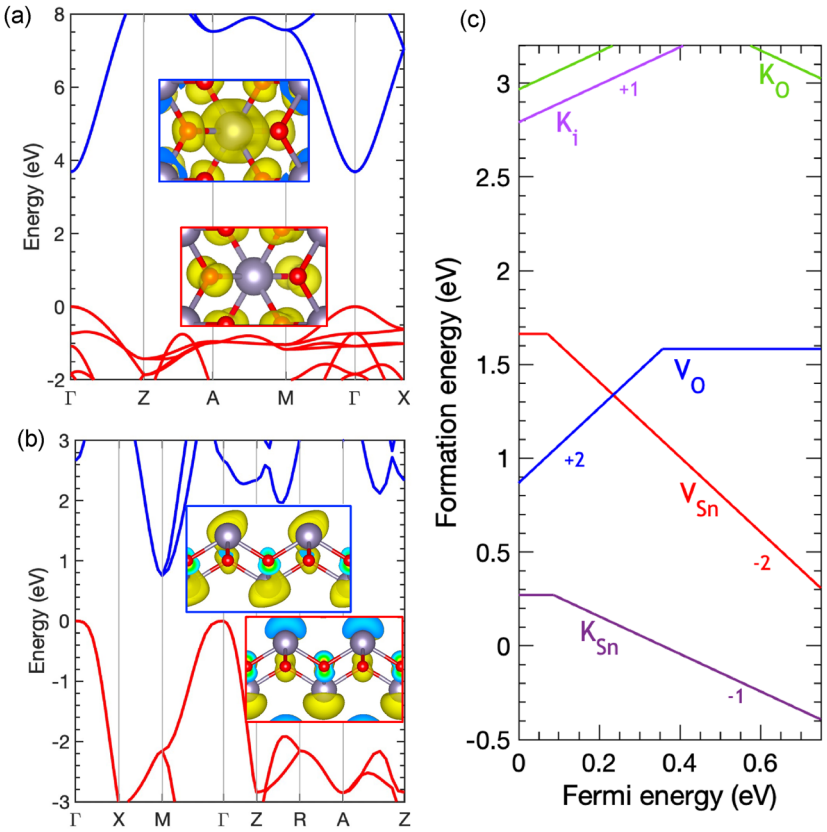

FIG. 1. [(a) and (b)] Calculated band structure, conduction band minimum (CBM), and valence band maximum (VBM) wavefunctions of SnO_2 and α-SnO, respectively, highlighting that the VBM of SnO_2 is composed of O 2*p* orbitals, while the VBM of α-SnO is composed of the hybridization between the O 2*p* and Sn 5*s* orbitals. The inset figures show the crystal structure and charge density of SnO_2 and α-SnO (Sn colored in blue–gray and O in red). The figures in the blue box display the charge density at the bottom of the conduction band, while the figures in the red box indicate the charge density at the top of the valence band. The value of the isosurface is chosen to be 10% of the highest charge density value. (c) Formation energy of potassium defects and intrinsic point defects as a function of the Fermi level under an extremely oxygen-poor condition [i.e., $\mu_O = \Delta H^f(\mathrm{SnO})$].

solubility of K_{Sn} in α-SnO. The resulting predicted solubility of K_{Sn} in α-SnO is 2×10^{20} atoms cm^{-3}, at which the Fermi energy is pinned at 86 meV above the valence band. This suggests that the theoretical limit of hole concentration (n_h) by potassium doping at room temperature is 8×10^{18} cm^{-3}. Although K_i and K_O are donor-type defects near the valence bands, they have formation energies more than 2.5 eV higher than that of K_{Sn}; therefore, self-compensation is not likely.

Next, we synthesize K-doped SnO thin films by *S*-MBE on YSZ (001) substrates with varied potassium doping concentrations by varying the temperature of the potassium effusion cell ($T_{K\ effusion\ cell}$). Figure 2(a) shows the x-ray diffraction of a representative K-doped α-SnO thin film ($T_{K\ effusion\ cell}$ = 260 °C). The film is (001) oriented with an epitaxial relationship of (001) SnO ‖ (001) YSZ and [100] SnO ‖ [110] YSZ in agreement with prior work.[27] Despite the incorporation of the potassium dopant, the SnO remains α-SnO, and no impurity phases are observed for the full range of dopant concentration studied in this work. Nonetheless, we observe the formation of (110)- and (101)-oriented α-SnO and K–Sn–O related compounds for $T_{K\ effusion\ cell}$ > 260 °C (Fig. S3). For all K-doped SnO thin films grown at $T_{K\ effusion\ cell}$ ≤ 260 °C, streaky reflection high-energy electron diffraction (RHEED) patterns are observed throughout the deposition [Fig. 2(c)], showing that the film is epitaxial and has a relatively smooth surface.

The atomic force microscopy image in Fig. 2(b) shows that our films remain smooth with an rms roughness of 2.2 nm after potassium doping. The supplementary material AFM image in Fig. S2 reveals the presence of growth spirals, where the diameter of grains ranges from 100–200 nm. Such spirals are often seen in the heteroepitaxial growth of layered materials, where the center of the spiral corresponds to where a threading dislocation with a screw component intersects the film surface.[79,80] The incoherent meeting of growth fronts is thought to be responsible for the nucleation of growth spirals in other layered materials[81–88] and is also the likely nucleation mechanism for the dislocations in these α-SnO films. We observed the density of growth spirals to increase with the flux of both SnO and potassium, which is consistent with the notion of an increased opportunity for the incoherent meeting of growth fronts as the growth rate increases. In the case of undoped SnO grown at a low SnO flux of 2×10^{12} molecules/(cm^2 s), the film has an rms roughness of 0.80 nm [see AFM image in Fig. S2(a)] and a spiral density of 1.3×10^8 cm^{-2}. When the SnO flux is increased to 1×10^{13} molecules/(cm^2 s), we observed a higher density of growth spirals (3.1×10^9 cm^{-2}) [Fig. S2(b)]. On the other hand, despite of low SnO flux [2×10^{12} molecules/(cm^2 s)], we observe a similarly high density of growth spirals around 1.5×10^9 cm^{-2} when potassium is supplied [Figs. S2(c) and 2(b)], suggesting that the increased potassium flux can accumulate at a growth front and

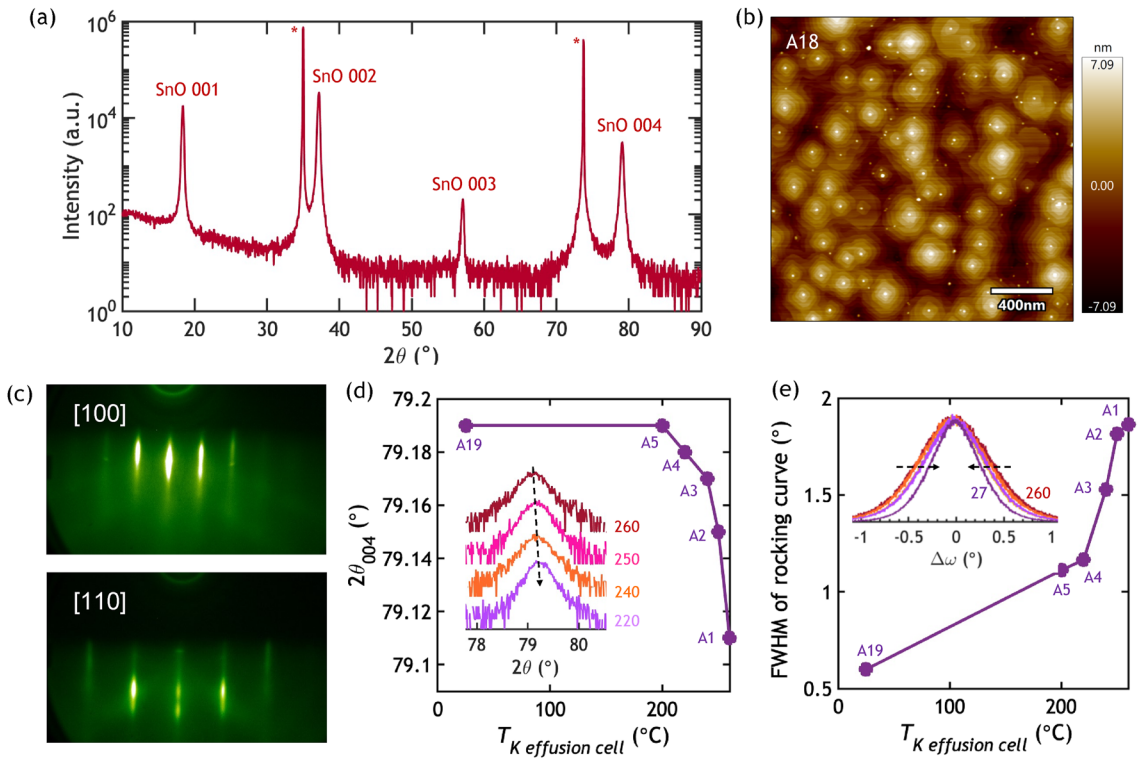

FIG. 2. (a) Symmetric θ-2θ x-ray diffraction scan, (b) atomic force microscopy, and (c) RHEED patterns observed along the [100] and [110] azimuths of a 60 nm-thick K-doped α-SnO thin film (Sample A18) grown on a YSZ (001) substrate with $T_{K\ effusion\ cell}$ = 260 °C. The peaks from the substrate are denoted by asterisks. (d) Out-of-plane planar spacing (d_{001}) of K-doped α-SnO thin films as a function of $T_{K\ effusion\ cell}$ determined from the 00ℓ α-SnO peaks in the symmetric x-ray diffraction scan. (e) FWHM of the x-ray rocking curve ($\Delta\omega$) of the 004 α-SnO peak as a function of $T_{K\ effusion\ cell}$.

locally decrease the growth rate of a section of the growth front, i.e., locally "poison" the advancement of the growth front. When the faster moving sections of the growth front later recombine beyond the poisoned region, they may no longer be aligned, giving rise to a screw dislocation.[81–85] We also observe that growth spirals facet along the in-plane ⟨100⟩ directions of α-SnO. The diameter of grains measured by AFM is used for the hole mobility calculation limited by grain boundary scattering.

In Fig. 2(d), we observe a gradual shift of the 2θ x-ray diffraction peak position of the K-doped α-SnO thin films to lower angle with increasing $T_{\text{K effusion cell}}$, which provides evidence for the incorporation of K in the α-SnO thin films. Due to the larger ionic radius of 4-coordinated K^+ (151 pm) compared to 4-coordinated Sn^{2+} (95 pm),[86] increasing the potassium doping concentration is expected to enlarge the lattice parameters of α-SnO. Experimentally, the out-of-plane planar spacing (d_{001}) of K-doped SnO thin films as a function of $T_{\text{K effusion cell}}$ is determined by a Nelson–Riley analysis[89] of the 2θ position of the 00ℓ α-SnO peaks in the symmetric x-ray diffraction scan. We measure d_{001} of the α-SnO thin films to increase by 0.16% at $T_{\text{K effusion cell}}$ = 250 °C. The measured strain is also plotted as a function of the K concentration in Fig. S4, where the K concentration is determined by SIMS measurement. The incorporation of the potassium dopant into α-SnO thin films is also evident from the broadening in the FWHM of the rocking curve measured for the α-SnO 002 peak in Fig. 2(e) as the temperature of the potassium effusion cell is increased. The FWHM of the rocking curve for the α-SnO thin film without dopants is 0.60°, but increases sharply with increasing potassium dopant concentration (1.86° at $T_{\text{K effusion cell}}$ = 260 °C). This indicates that the increased concentration of potassium dopants may cause local strains and perturb crystallinity due to the larger ionic size.

The atomic structure of K-doped α-SnO thin films is measured by scanning transmission electron microscopy (STEM) in Fig. 3(a). From the high-angle annular dark-field (HAADF) STEM image, it is hard to distinguish the interface between the K-doped α-SnO layer and the undoped α-SnO layer (10 nm away from the SnO/YSZ interface), demonstrating that good crystallinity is maintained in the α-SnO thin films despite the incorporation of potassium dopants. No evidence of dopant clustering or the formation of an impurity phase is observed.

To determine the concentration of the potassium dopants, we employed SIMS. Immediately prior to the SIMS analysis, the samples were cleaned with methanol followed by absolute ethanol to remove any potassium contamination on the film surface. Figure 3(b) shows the measured potassium concentration profile as a function of film depth, where the film surface is positioned at 0 and the K-doped SnO/SnO interface is indicated by the arrows. Calibration standards made by ion implanting potassium into undoped α-SnO films grown under the same *S*-MBE conditions were used to quantify the potassium concentration in the SIMS measurements. The position of the interface to the (001) YSZ substrate was determined by monitoring the yttrium signal in SIMS. Clearly, increasing $T_{\text{K effusion cell}}$ increases the concentration of potassium (except for $T_{\text{K effusion cell}}$ = 250 °C), suggesting that the dopant concentration can be roughly controlled

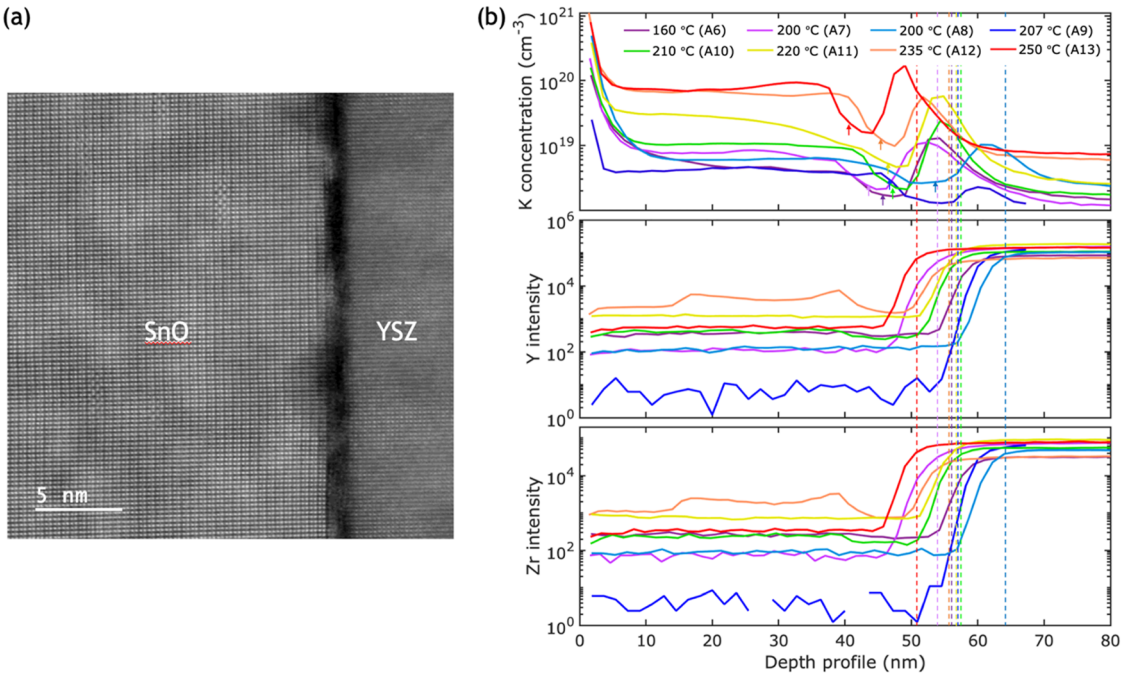

FIG. 3. (a) Scanning transmission electron microscopy image of a K-doped α-SnO thin film ($T_{\text{K effusion cell}}$ = 260 °C) grown on a YSZ (001) substrate. (b) Potassium concentration profile measured by SIMS as a function of film depth for α-SnO films grown at varying temperatures of the potassium effusion cell, compared with the intensity of Y and Zr. The position of the interface between the YSZ substrate and the α-SnO layer is marked by dotted vertical lines of the same color as the corresponding K-doped sample.

by the effusion cell temperature. The maximum concentration of potassium measured from SIMS is 5.3 × 10^{19} cm^{-3} at $T_{K\ effusion\ cell}$ = 235 °C, which is close to the solubility limit of potassium predicted by theory. We further fabricated a SIMS stack composed of three layers of 50 nm-thick undoped α-SnO separated by three layers of 50 nm-thick K-doped α-SnO with varied $T_{K\ effusion\ cell}$ (233 °C, 246 °C, and 260 °C, respectively) and measured the resulting SIMS profile in Fig. S7. The potassium concentration is clearly distinguished for each layer and increases with $T_{K\ effusion\ cell}$, verifying that the potassium concentration can be controlled by the effusion cell temperature.

Next, Hall effect measurements are carried out on the K-doped α-SnO thin films with varied potassium concentrations (Fig. 4). We first observe that the unintentionally doped α-SnO thin films grown under the same conditions as the K-doped films exhibit hole conductivity (ρ = 2.80 Ω cm) with n_h = 5 (±1) × 10^{17} cm^{-3} and μ = 8 ± 2 cm^2 V^{-1} s^{-1}, which may originate from the presence of native acceptor-type defects, such as tin vacancies.[12] For K-doped α-SnO thin films, we start to observe a noticeable change of hole conductivity at $T_{K\ effusion\ cell}$ ≥ 200 °C. At 200 °C ≤ $T_{K\ effusion\ cell}$ ≤ 250 °C, the resistivity decreases, and the hole density increases exponentially with the cell temperature [Figs. 4(a) and 4(b)]. The exponential increase of n_h with $T_{K\ effusion\ cell}$ is expected due to the exponential dependence of molecular beam flux on cell temperature. The measured hole concentration of the K-doped α-SnO thin films at $T_{K\ effusion\ cell}$ = 250 °C is 1.4 × 10^{19} cm^{-3}, ~35 times higher than the undoped α-SnO thin films. In the measured doping range (4.3 × 10^{17}–1.5 × 10^{19} cm^{-3}), the hole mobility decreases monotonically (from 7.7 ± 2.4 to 3.7 ± 0.1 cm^2 V^{-1} s^{-1}) with carrier density. This can be explained by ionized impurity scattering, which is the dominant scattering mechanism of α-SnO in the high carrier concentration range (n_h > 10^{17} cm^{-3}).[10] The successful control of hole carriers by changing the potassium dopant concentration demonstrates that K^+ substitutes for Sn^{2+} in α-SnO thin films, donating free holes, which aligns with our theory result.

In Fig. 4(b), the measured mobility is compared with the calculated mobility. Here, we calculated the room-temperature mobility of α-SnO under various defect concentrations. Our result presents the calculated hole mobility of α-SnO in the doping concentration range of 1 × 10^{17}–1 × 10^{20} cm^{-3}, showing that the charged impurity scattering (K^+ as the charged defect) can significantly degrade the phonon-limited intrinsic mobility.

Figure 4(c) presents a temperature-dependent Hall measurement on an undoped α-SnO film and K-doped α-SnO films with varied $T_{K\ effusion\ cell}$. A plot of ln(n_h) vs 1000/T nicely fits to a linear equation, where the slope indicates the ionization energy of holes. The measured ionization energies of the K-doped α-SnO samples vary from 11.1 ± 0.2 to 20.4 ± 0.1 meV depending on the doping concentration, indicating that potassium is a shallow acceptor. A low ionization energy might be expected in films that are degenerately doped, where an impurity band can form, but even in films with low potassium doping (e.g., the sample with a potassium concentration of 2.0 × 10^{18} cm^{-3} and a hole concentration at room temperature of 5.8 × 10^{17} cm^{-3}), we see ionization energies in the

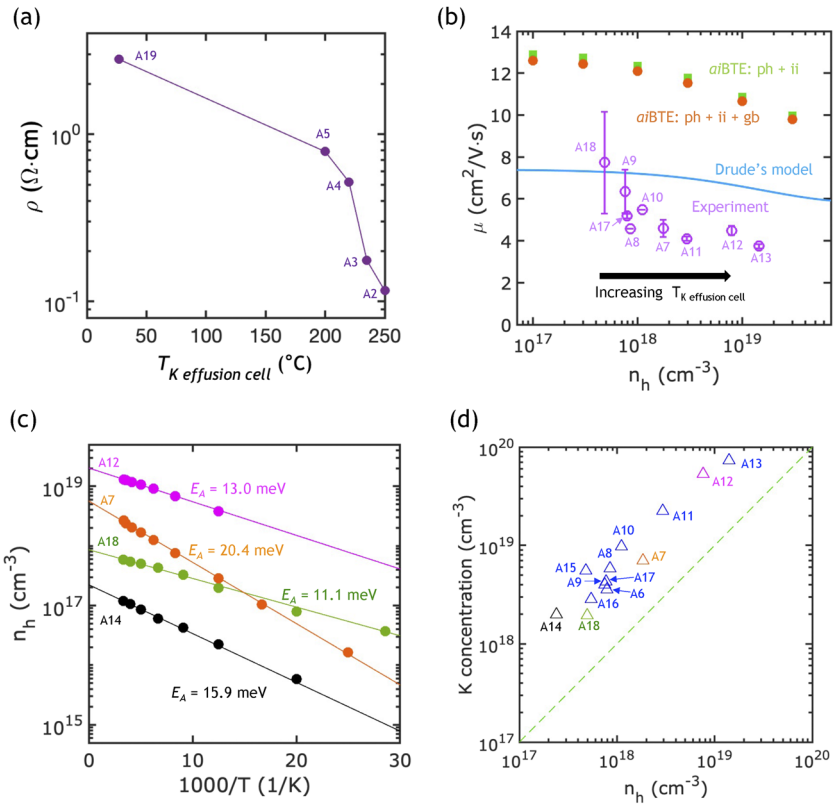

FIG. 4. (a) Measured resistivity of K-doped α-SnO thin films as a function of $T_{K\ effusion\ cell}$. (b) Hole mobility (μ) vs hole density (n_h) obtained from the Hall effect measurements for the K-doped α-SnO thin films with varied $T_{K\ effusion\ cell}$, compared with the theoretical values calculated with phonon, ionized impurity, and grain boundary scattering (orange), theoretical values calculated with phonon and ionized impurity scattering (light green), and theoretical values calculated by Drude's model (light blue). (c) Temperature-dependent hole concentration in an undoped α-SnO sample (black, sample A14) and the K-doped α-SnO samples with varied doping concentrations (green, sample A18; orange, sample A7; and magenta, sample A12). (d) Potassium concentration measured by SIMS vs the hole carrier concentration measured at room temperature by the Hall effect. The data points with different edge colors indicate the same four samples used for temperature-dependent Hall measurement in (c).

10–20 meV range, indicating that potassium is intrinsically a shallow dopant in α-SnO. Note that potassium has the lowest ionization energy measured for any dopant in α-SnO. The ionization energies measured for prior dopants were 43 meV at a gallium concentration of 7×10^{19} cm^{-3},[20,21] 52 meV for a gallium concentration of 2×10^{20} cm^{-3},[20,21] and 20 meV for a sodium concentration of 5×10^{20} cm^{-3}.[21] The difference between the calculated ionization energies and measured ionization energies is due to the inherent error bars of ionization energies from the first-principles calculation. In the case of a p-type GaN, the calculated ionization energies of the acceptor dopants are 260 meV for magnesium,[90] 230 meV for zinc,[91] and 650 meV for cadmium,[92] while the experimental values are 170–230 meV for magnesium,[93,94] 220–328 meV for zinc,[95,96] and 550 meV for cadmium.[95] This is consistent with the calculated ionization energies having an uncertainty of about ±100 meV.[91]

The measured ionization energy of an undoped α-SnO film is 15.9 ± 0.2 meV. This is surprising considering that Egbo *et al.*[21] have found the ionization energies of their unintentionally doped α-SnO films grown by plasma-assisted MBE to be 72 meV and Kwok *et al.*[21] have found that of 40 meV for their undoped α-SnO films grown by magnetron sputtering. To be sure that our samples were not inadvertently contaminated by potassium, the unintentionally doped α-SnO film measured in Fig. 4(c) was grown in a different MBE growth chamber, in which potassium has never been used on substrate holders also never exposed to potassium, using the same growth conditions and *S*-MBE as the other samples in this study. This leads us to conclude that the electrically active defects in unintentionally doped α-SnO grown by *S*-MBE are quite different from those grown by plasma-assisted MBE. Furthermore, our results show the dominant acceptor defects in our unintentionally doped α-SnO to be shallow, possibly V_{Sn} acceptors, which align with our theory results that predict a relatively low acceptor ionization energy of V_{Sn}.

Figure 4(d) compares the hole carrier concentration with the average potassium concentration measured by SIMS for ten K-doped α-SnO samples. The average potassium concentration of each film is determined by integrating the potassium concentration values measured by SIMS [Fig. 3(b)] from the minimum after the surface peak to the end of the K-doped portion of the film and dividing it by the thickness. The carrier concentration generally increases with increasing potassium concentration, suggesting that potassium acts as an acceptor dopant in α-SnO as predicted by the DFT. The average electrical activation of potassium (i.e., carrier concentration/potassium concentration) is only 17.0%, though it ranges as low as 8.7% and high as 26.4%. The variation in the concentration of active dopants may be explained by an uncontrolled trap state in our films that needs to be better controlled to realize the full potential of potassium as a dopant in α-SnO films.

We also tested the temperature and time stability of the undoped and K-doped α-SnO thin films in Figs. S5 and S6. A thermal stability test was carried out by placing the sample on a hot plate at each target temperature for 10 min. After cooling the sample down to room temperature, Hall effect measurements were performed. This process was repeated by subsequently heating the sample to the next temperature, holding for 10 min, cooling, and then measuring. We observed that the K-doped *α*-SnO thin films do not show a noticeable change in mobility or hole carrier concentration after annealing the samples up to 300 °C [Figs. S5(a) and S5(b)]. Nonetheless, Sn 200 and SnO_2 110 impurity peaks are observed in XRD after post-annealing at 300 °C, indicating that phase decomposition is likely occurring [Fig. S5(c)]. On the other hand, for the undoped *α*-SnO thin films, the mobility degrades, and the carrier concentration increases at annealing temperatures >200 °C. Nevertheless, the films remain epitaxial without noticeable impurity peaks in the XRD. A time stability test was also performed for the undoped α-SnO thin films and K-doped α-SnO thin films with varied $T_{\text{K effusion cell}}$ (Fig. S6). The K-doped α-SnO thin films with $T_{\text{K effusion cell}}$ in the range of 140 and 250 °C maintain relatively stable electrical properties as a function of time when stored at room temperature in a desiccator purged with nitrogen for ~1 year after deposition. On the other hand, the undoped SnO exhibits noticeable degradation of mobility with time.

Divided spectral range analysis of measured ellipsometric spectra has been used to obtain the structural and optical property parameters (see the supplementary material Table S3) and determine the optical response in terms of spectra in ε [Figs. 5(a) and 5(b)]. These epitaxially grown α-SnO films are tetragonal and uniaxially anisotropic with the optic axis oriented normal to the substrate surface. Even though multiple angles of incidence ellipsometry measurements are employed, sensitivity to this optical anisotropy is weak,[77] and the films are treated as isotropic. All of the films

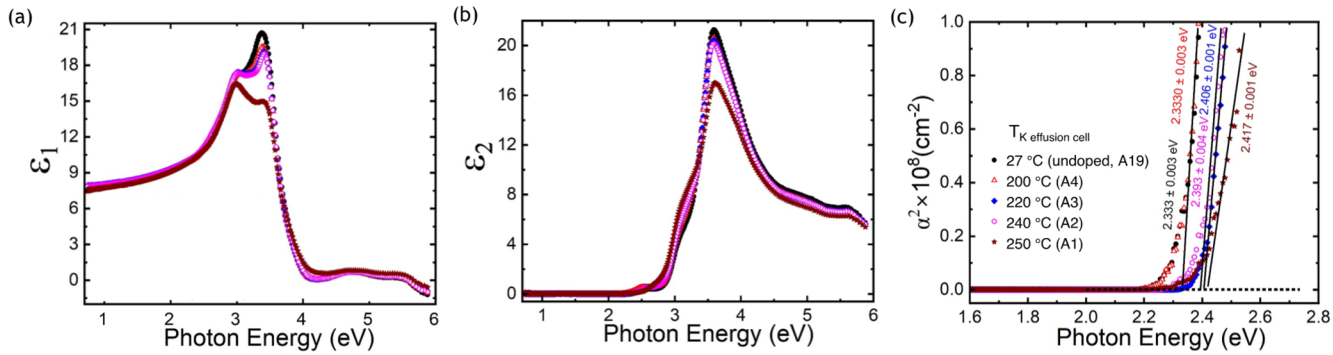

FIG. 5. (a) and (b) Spectra in ε of epitaxial α-SnO films from 0.73 to 5.87 eV. (c) Tauc plots to determine the optical bandgap, which varies negligibly (<0.09 eV) with doping level.

have a 15–20 nm thick lower optical density layer near the substrate/film interface, except the film deposited with $T_{\text{K effusion cell}}$ = 250 °C. This observation is consistent with the SIMS [Fig. 3(b)], including the deviation of the $T_{\text{K effusion cell}}$ = 250 °C from the trend in K-concentration from the SIMS and the lack of an interfacial layer identified from spectroscopic ellipsometry attributed to poor optical contrast between this interfacial layer and the bulk film. The surface and bulk film layer thicknesses are approximately consistent throughout all the films. The 5–6 nm thick surface layers from ellipsometry exceed the 2.2 nm rms roughness from AFM. These optically determined surface layers may consist of contributions from surface roughness features, different bonding configurations at the surface, absorbed species from the ambient, or a combination of these effects leading to the thickness discrepancy. From spectra in ε above gap, critical point transitions are observed at 3.1 and 3.5 eV for all samples, with the critical point located around 3.5 eV being the most prominent feature.

The absorption coefficient (α) spectra are derived from $\alpha = 4\pi k/\lambda$, where k is obtained from $\varepsilon = (n + ik)^2$ and λ is the photon wavelength. The direct optical bandgap of these films is determined using the Tauc plots of the extrapolation of α^2 to zero over a range of α from 0.54×10^4 to 1×10^4 cm^{-1} [Fig. 5(c)]. The optical bandgaps increase from 2.33 eV for the films grown with $T_{\text{K effusion cell}}$ = 27 and 200 °C to 2.42 eV at $T_{\text{K effusion cell}}$ = 250 °C. The optical bandgap energies from 2.6 to 2.7 eV have been reported for SnO; however, a higher absorption coefficient range of 0.5×10^5–2×10^5 cm^{-1} was used for extrapolation.[27,77,97]

The optical gap values and low values of the imaginary part of ε (ε_2) indicate that these films are not substantially absorbing from the near infrared through the middle visible range from 0.73 to ~2.4 eV (1700 to ~520 nm). Substantial absorption in ε_2 begins near ~2.8 eV (~440 nm), indicating that these SnO layers will still be optically transparent if sufficiently thin (<1 μm).

CONCLUSIONS

In conclusion, we find that potassium doping can be used to control the p-type carrier concentration of α-SnO thin films. The first-principles calculation predicted that potassium is an acceptor that is not compensated by native defects. Single-crystalline K-doped α-SnO thin films were then synthesized by *S*-MBE at 375 °C. Potassium dopants are incorporated during the deposition and the doping concentration is varied by changing the temperature of the potassium effusion cell. Our transport data from the Hall measurement indicate that the hole concentration of α-SnO can be controlled by potassium doping by ~2 orders of magnitude (4.8×10^{17}–1.5×10^{19} cm^{-3}) with a relatively small degradation of mobility (3.7–7.7 cm^2 V^{-1} s^{-1}), which leads to the modulation of hole resistivity from 2.8 to 0.12 Ω cm. The SIMS confirms that potassium has a high solid solubility in the K-doped SnO, 2.4×10^{20} cm^{-3}. Temperature-dependent Hall measurements reveal that potassium is a shallow acceptor in α-SnO with an ionization energy ranging from 11.1 ± 0.2 to 20.4 ± 0.1 meV. The unintentionally doped films were also found to have a shallow ionization energy (15.9 ± 0.2 meV), which we attribute to the V_{Sn} defects. Spectroscopic ellipsometry determined that optical bandgaps range from 2.33 to 2.42 eV with increasing K-doping, indicating that optical transparency is maintained. The successful modulation of p-type conduction and low deposition temperature may allow α-SnO to be used for p-channel transistors made at the BEOL.

SUPPLEMENTARY MATERIAL

The supplementary material provides additional figures and tables that support the findings of this study, including DFT and GW band structures, atomic force microscopy images, x-ray diffraction of K-doped α-SnO thin films with high K effusion cell temperature, strain analysis, thermal and time stability analysis, measurement of a SIMS stack, sample information in this work, calculated dynamic quadrupole tensors of SnO for mobility calculation, and optical property parameters of the undoped and K-doped α-SnO thin films.

ACKNOWLEDGMENTS

This work was primarily supported by SUPREME, one of the seven centers sponsored by the Semiconductor Research Corporation (SRC) and DARPA under the Joint University Microelectronics Program 2.0 (JUMP 2.0). V.-A.H. and F.G. are supported by the Computational Materials Science program of U.S. Department of Energy, Office of Science, Basic Energy Sciences under Award No. DE-SC0020129 (EPW software development). Computational resources were provided by the National Energy Research Scientific Computing Center (a DOE Office of Science User Facility supported under Contract No. DE-AC02-05CH11231), the Argonne Leadership Computing Facility (a DOE Office of Science User Facility supported under Contract No. DE-AC02-06CH11357), and the Texas Advanced Computing Center (TACC) at the University of Texas at Austin. M.K.I.S. and M.D.W. acknowledge support from the National Science Foundation (Grant No. PREM-DMR-2122147) and the Office of Naval Research HBCU/MI Faculty Start-up Program in Materials Physics (Grant No. N00014-21-1-2823). Materials synthesis was performed partly in a facility supported by the NSF [Platform for the Accelerated Realization, Analysis, and Discovery of Interface Materials (PARADIM)] under Cooperative Agreement No. DMR-2039380. Substrate preparation was performed, in part, at the Cornell NanoScale Facility, a member of the National Nanotechnology Coordinated Infrastructure (NNCI), which is supported by the NSF (Grant No. NNCI-2025233). The authors thank Steven Button for his assistance with substrate preparation.

AUTHOR DECLARATIONS

Conflict of Interest

The author D.G.S. was granted the U.S. Patent No. 11,462,402 (4 October 2022) with the title "Suboxide Molecular-Beam Epitaxy and Related Structures."

Author Contributions

S.C., S.L., A.P., and M.K.I.S. contributed equally to this work.

Sieun Chae: Conceptualization (equal); Data curation (equal); Formal analysis (equal); Writing – original draft (equal). **Seungmin Lee**: Data curation (equal); Formal analysis (equal); Validation (equal); Writing – review & editing (equal). **Anna Park**: Data curation

(equal); Formal analysis (equal). **M. K. Indika Senevirathna**: Data curation (equal); Formal analysis (equal); Writing – review & editing (equal). **Yufan Feng**: Data curation (equal); Formal analysis (equal). **Venkanna Kanneboina**: Data curation (equal); Formal analysis (equal); Writing – review & editing (equal). **Viet-Anh Ha**: Data curation (equal); Formal analysis (equal); Writing – review & editing (equal). **Yaoqiao Hu**: Data curation (equal); Writing – review & editing (equal). **Chaojie Du**: Data curation (equal); Formal analysis (equal); Writing – review & editing (equal). **Matthew Barone**: Formal analysis (equal); Writing – review & editing (equal). **Vladimir Protasenko**: Writing – review & editing (equal). **Yilin Evan Li**: Data curation (equal); Writing – review & editing (equal). **Nikolas Podraza**: Data curation (equal); Writing – review & editing (equal). **Kedar Johnson**: Data curation (equal); Writing – review & editing (equal). **Debdeep Jena**: Writing – review & editing (equal). **Huili G. Xing**: Writing – review & editing (equal). **Xiaoqing Pan**: Writing – review & editing (equal). **Kyeongjae Cho**: Writing – review & editing (equal). **Feliciano Giustino**: Writing – review & editing (equal). **Michael D. Williams**: Writing – review & editing (equal). **Darrell G. Schlom**: Funding acquisition (equal); Project administration (equal); Resources (equal); Supervision (equal); Validation (equal); Writing – review & editing (equal).

DATA AVAILABILITY

The data that support the findings of this study are available within the article. Additional data related to the film growth and structural characterization by RHEED, XRD, AFM, and chemical characterization by SIMS are available at https://doi.org/10.34863/4cdx-6j33. Any additional data connected to the study are available from the corresponding author upon reasonable request.

REFERENCES

[1] K. Nomura, H. Ohta, A. Takagi, T. Kamiya, M. Hirano, and H. Hosono, "Room-temperature fabrication of transparent flexible thin-film transistors using amorphous oxide semiconductors," Nature **432**(7016), 488–492 (2004).

[2] T. Kamiya and H. Hosono, "Material characteristics and applications of transparent amorphous oxide semiconductors," NPG Asia Mater. **2**(1), 15–22 (2010).

[3] M. M. S. Aly, M. Gao, G. Hills, C.-S. Lee, G. Pitner, M. M. Shulaker, J. Bokor, F. Franchetti, K. E. Goodson, C. Kozyrakis, I. Markov, K. Olukotun, L. Pileggi, E. Pop, J. Rabaey, C. Ré, H.-S. Philip Wong, and S. Mitra, "Energy-efficient abundant-data computing: The N3XT 1,000x," Computer **48**(12), 24–33 (2015).

[4] S. Salahuddin, K. Ni, and S. Datta, "The era of hyper-scaling in electronics," Nat. Electron. **1**(8), 442 (2018).

[5] S. Datta, S. Dutta, B. Grisafe, J. Smith, S. Srinivasa, and H. Ye, "Back-end-of-line compatible transistors for monolithic 3-D integration," IEEE Micro **39**(6), 8–15 (2019).

[6] A. P. Chandrakasan and R. W. Brodersen, "Minimizing power consumption in digital CMOS circuits," High-Perform. Syst. Des.: Circuits Logic **83**(4), 498–523 (1995).

[7] H. Kawazoe, H. Yanagi, K. Ueda, and H. Hosono, "Transparent *p*-type conducting oxides: Design and fabrication of *p-n* heterojunction," MRS Bull. **25**, 28–36 (2000).

[8] H. Hosono, "Exploring electro-active functionality of transparent oxide materials," Jpn. J. Appl. Phys. **52**(9R), 090001 (2013).

[9] G. Hautier, A. Miglio, G. Ceder, G.-M. Rignanese, and X. Gonze, "Identification and design principles of low hole effective mass *p*-type transparent conducting oxides," Nat. Commun. **4**, 2292 (2013).

[10] M. Minohara, A. Samizo, N. Kikuchi, K. K. Bando, Y. Yoshida, and Y. Aiura, "Tailoring the hole mobility in SnO films by modulating the growth thermodynamics and kinetics," J. Phys. Chem. C **124**(2), 1755–1760 (2020).

[11] C. W. Shih, A. Chin, C. F. Lu, and W. F. Su, "Remarkably high hole mobility metal-oxide thin-film transistors," Sci. Rep. **8**(1), 889 (2018).

[12] J. B. Varley, A. Schleife, A. Janotti, and C. G. Van De Walle, "Ambipolar doping in SnO," Appl. Phys. Lett. **103**(8), 082118 (2013).

[13] A. Togo, F. Oba, I. Tanaka, and K. Tatsumi, "First-principles calculations of native defects in tin monoxide," Phys. Rev. B **74**(19), 195128 (2006).

[14] M. Graužinytė, S. Goedecker, and J. A. Flores-Livas, "Towards bipolar tin monoxide: Revealing unexplored dopants," Phys. Rev. Mater. **2**(10), 104604 (2018).

[15] W. Guo, L. Fu, Y. Zhang, K. Zhang, L. Y. Liang, Z. M. Liu, H. T. Cao, and X. Q. Pan, "Microstructure, optical, and electrical properties of *p*-type SnO thin films," Appl. Phys. Lett. **96**(4), 042113 (2010).

[16] H. Hosono, Y. Ogo, H. Yanagi, and T. Kamiya, "Bipolar conduction in SnO thin films," Electrochem. Solid-State Lett. **14**(1), H13 (2011).

[17] L. Y. Liang, Z. M. Liu, H. T. Cao, W. Y. Xu, X. L. Sun, H. Luo, and K. Cang, "The structural, optical and electrical properties of Y-doped SnO thin films and their p-type TFT application," J. Phys. D:Appl. Phys. **45**(8), 085101 (2012).

[18] S. Yim, T. Kim, B. Yoo, H. Xu, Y. Youn, S. Han, and J. K. Jeong, "Lanthanum doping enabling high drain current modulation in a p-type tin monoxide thin-film transistor," ACS Appl. Mater. Interfaces **11**(50), 47025–47036 (2019).

[19] L. Qin, S. Yuan, Z. Chen, X. Bai, J. Xu, L. Zhao, W. Zhou, Q. Wang, J. Chang, and J. Sun, "Solution-processed transparent p-type orthorhombic K doped SnO films and their application in a phototransistor," Nanoscale **14**(37), 13763–13770 (2022).

[20] C. K. G. Kwok, Y. Wang, K. Egbo, and K. M. Yu, "Improving the p-type conductivity and transparency of pure phase SnO by Ga and Na doping," J. Phys. Chem. C **126**(44), 18963–18971 (2022).

[21] K. Egbo, J. Lähnemann, A. Falkenstein, J. Varley, and O. Bierwagen, "Acceptor and compensating donor doping of single crystalline SnO (001) films grown by molecular beam epitaxy and its perspectives for optoelectronics and gas-sensing," Appl. Phys. Lett. **122**(12), 122101 (2023).

[22] S. Nam, S. J. Lee, J. E. Pi, J. H. Yang, C. S. Hwang, and S. H. Cho, "The potassium-assisted p-type characteristics of tin oxide in solution-processed high-performance metal oxide thin-film transistors," Phys. Status Solidi A **218**(18), 2170052 (2021).

[23] G. Kresse and J. Furthmüller, "Efficient iterative schemes for *ab initio* total-energy calculations using a plane-wave basis set," Phys. Rev. B **54**(16), 11169–11186 (1996).

[24] J. P. Perdew, K. Burke, and M. Ernzerhof, "Generalized gradient approximation made simple," Phys. Rev. Lett. **77**, 3865–3868 (1996).

[25] J. Heyd, G. E. Scuseria, and M. Ernzerhof, "Hybrid functionals based on a screened Coulomb potential," J. Chem. Phys. **118**(18), 8207–8215 (2003).

[26] F. Izumi, "Pattern-fitting structure refinement of tin(II) oxide," J. Solid State Chem. **38**, 381–385 (1981).

[27] Y. Ogo, H. Hiramatsu, K. Nomura, H. Yanagi, T. Kamiya, M. Hirano, and H. Hosono, "*p*-channel thin-film transistor using *p*-type oxide semiconductor, SnO," Appl. Phys. Lett. **93**(3), 032113 (2008).

[28] C. Freysoldt, B. Grabowski, T. Hickel, J. Neugebauer, G. Kresse, A. Janotti, and C. G. Van De Walle, "First-principles calculations for point defects in solids," Rev. Mod. Phys. **86**(1), 253–305 (2014).

[29] C. Freysoldt, J. Neugebauer, and C. G. Van De Walle, "Fully *ab initio* finite-size corrections for charged-defect supercell calculations," Phys. Rev. Lett. **102**, 016402 (2009).

[30] Y. Hu, J. Hwang, Y. Lee, P. Conlin, D. G. Schlom, S. Datta, and K. Cho, "First principles calculations of intrinsic mobilities in tin-based oxide semiconductors SnO, SnO_2, and Ta_2SnO_6," J. Appl. Phys. **126**(18), 185701 (2019).

[31] E. Conwell and V. F. Weisskopf, "Theory of impurity scattering in semiconductors," Phys. Rev. **77**, 388 (1950).

[32] M. Lundstrom, "Fundamentals of carrier transport," Meas. Sci. Technol. **13**, 230 (2002).

[33] S. Poncé, E. R. Margine, and F. Giustino, "Towards predictive many-body calculations of phonon-limited carrier mobilities in semiconductors," Phys. Rev. B **97**(12), 121201 (2018).

[34]S. Poncé, W. Li, S. Reichardt, and F. Giustino, "First-principles calculations of charge carrier mobility and conductivity in bulk semiconductors and two-dimensional materials," Rep. Prog. Phys. **83**(3), 036501 (2020).
[35]F. Giustino, "Electron-phonon interactions from first principles," Rev. Mod. Phys. **89**(1), 015003 (2017).
[36]H. Lee, S. Poncé, K. Bushick, S. Hajinazar, J. Lafuente-Bartolome, J. Leveillee, C. Lian, J. M. Lihm, F. Macheda, H. Mori, H. Paudyal, W. H. Sio, S. Tiwari, M. Zacharias, X. Zhang, N. Bonini, E. Kioupakis, E. R. Margine, and F. Giustino, "Electron–phonon physics from first principles using the EPW code," npj Comput. Mater. **9**, 156 (2023).
[37]C. Verdi and F. Giustino, "Fröhlich electron-phonon vertex from first principles," Phys. Rev. Lett. **115**(17), 176401 (2015).
[38]J. Sjakste, N. Vast, M. Calandra, and F. Mauri, "Wannier interpolation of the electron-phonon matrix elements in polar semiconductors: Polar-optical coupling in GaAs," Phys. Rev. B:Condens. Matter Mater. Phys. **92**(5), 054307 (2015).
[39]J. Park, J. J. Zhou, V. A. Jhalani, C. E. Dreyer, and M. Bernardi, "Long-range quadrupole electron-phonon interaction from first principles," Phys. Rev. B **102**(12), 125203 (2020).
[40]G. Brunin, H. P. C. Miranda, M. Giantomassi, M. Royo, M. Stengel, M. J. Verstraete, X. Gonze, G. M. Rignanese, and G. Hautier, "Phonon-limited electron mobility in Si, GaAs, and GaP with exact treatment of dynamical quadrupoles," Phys. Rev. B **102**, 094308 (2020).
[41]M. Royo and M. Stengel, "First-principles theory of spatial dispersion: Dynamical quadrupoles and flexoelectricity," Phys. Rev. X **9**(2), 021050 (2019).
[42]J. Leveillee, X. Zhang, E. Kioupakis, and F. Giustino, "*Ab initio* calculation of carrier mobility in semiconductors including ionized-impurity scattering," Phys. Rev. B **107**, 125207 (2023).
[43]L. Lindsay, D. A. Broido, and N. Mingo, "Lattice thermal conductivity of single-walled carbon nanotubes: Beyond the relaxation time approximation and phonon-phonon scattering selection rules," Phys. Rev. B **80**(12), 125407 (2009).
[44]N. Mingo and D. A. Broido, "Length dependence of carbon nanotube thermal conductivity and the 'problem of long waves,'" Nano Lett. **5**(7), 1221–1225 (2005).
[45]L. Lindsay, D. A. Broido, and N. Mingo, "Diameter dependence of carbon nanotube thermal conductivity and extension to the graphene limit," Phys. Rev. B **82**, 161402(R) (2010).
[46]H. Lee, Y. Zhou, S. Jung, H. Li, Z. Cheng, J. He, J. Chen, P. Sokalski, A. Dolocan, R. Gearba-Dolocan, K. C. Matthews, F. Giustino, J. Zhou, and L. Shi, "High-pressure synthesis and thermal conductivity of semimetallic θ-tantalum nitride," Adv. Funct. Mater. **33**, 2212957 (2023).
[47]P. Giannozzi, S. Baroni, N. Bonini, M. Calandra, R. Car, C. Cavazzoni, D. Ceresoli, G. L. Chiarotti, M. Cococcioni, I. Dabo, A. D. Corso, S. De Gironcoli, U. Gerstmann, C. Gougoussis, A. Kokalj, M. Lazzeri, L. Martin-samos, N. Marzari, F. Mauri, R. Mazzarello, S. Paolini, A. Pasquarello, L. Paulatto, and C. Sbraccia, "QUANTUM ESPRESSO: A modular and open-source software project for quantum simulations of materials," J. Phys.: Condens. Matter **21**, 395502 (2009).
[48]P. Giannozzi, O. Andreussi, T. Brumme, O. Bunau, M. B. Nardelli, M. Calandra, R. Car, C. Cavazzoni, D. Ceresoli, M. Cococcioni, N. Colonna, I. Carnimeo, A. Dar Corso, S. de Gironcoli, P. Delugas, R. A. DiStasio, Jr., A. Ferretti, A. Floris, G. Fratesi, G. Fugallo, R. Gebauer, U. Gerstmann, F. Giustino, T. Gorni, J. Jia, M. Kawamura, H.-Y. Ko, A. Kokalj, E. Küçükbenli, M. Lazzeri, M. Marsili, N. Marzari, F. Mauri, N. L. Nguyen, H.-V. Nguyen, A. Otero-de-la-Roza, L. Paulatto, S. Poncé, D. Rocca, R. Sabatini, B. Santra, M. Schlipf, A. P. Seitsonen, A. Smogunov, I. Timrov, T. Thonhauser, P. Umari, N. Vast, X. Wu, and S. Baroni, "Advanced capabilities for materials modelling with QUANTUM ESPRESSO," J. Phys.: Condens. Matter **29**(46), 465901 (2017).
[49]D. R. Hamann, "Optimized norm-conserving Vanderbilt pseudopotentials," Phys. Rev. B **88**, 085117 (2013).
[50]M. J. van Setten, M. Giantomassi, E. Bousquet, M. J. Verstraete, D. R. Hamann, X. Gonze, and G. M. Rignanese, "The PSEUDODOJO: Training and grading a 85 element optimized norm-conserving pseudopotential table," Comput. Phys. Commun. **226**, 39–54 (2018).
[51]M. S. Hybertsen and S. G. Louie, "Electron correlation in semiconductors and insulators: Band gaps and quasiparticle energies," Phys. Rev. B **34**(8), 5390–5413 (1986).
[52]J. Deslippe, G. Samsonidze, D. A. Strubbe, M. Jain, M. L. Cohen, and S. G. Louie, "BerkeleyGW: A massively parallel computer package for the calculation of the quasiparticle and optical properties of materials and nanostructures," Comput. Phys. Commun. **183**(6), 1269–1289 (2012).
[53]X. Gonze, B. Amadon, G. Antonius, F. Arnardi, L. Baguet, J. M. Beuken, J. Bieder, F. Bottin, J. Bouchet, E. Bousquet, N. Brouwer, F. Bruneval, G. Brunin, T. Cavignac, J. B. Charraud, W. Chen, M. Côté, S. Cottenier, J. Denier, G. Geneste, P. Ghosez, M. Giantomassi, Y. Gillet, O. Gingras, D. R. Hamann, G. Hautier, X. He, N. Helbig, N. Holzwarth, Y. Jia, F. Jollet, W. Lafargue-Dit-Hauret, K. Lejaeghere, M. A. L. Marques, A. Martin, C. Martins, H. P. C. Miranda, F. Naccarato, K. Persson, G. Petretto, V. Planes, Y. Pouillon, S. Prokhorenko, F. Ricci, G. M. Rignanese, A. H. Romero, M. M. Schmitt, M. Torrent, M. J. van Setten, B. Van Troeye, M. J. Verstraete, G. Zérah, and J. W. Zwanziger, "The ABINITproject: Impact, environment and recent developments," Comput. Phys. Commun. **248**, 107042 (2020).
[54]A. B. Mei, L. Miao, M. J. Wahila, G. Khalsa, Z. Wang, M. Barone, N. J. Schreiber, L. E. Noskin, H. Paik, T. E. Tiwald, Q. Zheng, R. T. Haasch, D. G. Sangiovanni, L. F. J. Piper, and D. G. Schlom, "Adsorption-controlled growth and properties of epitaxial SnO films," Phys. Rev. Mater. **3**(10), 105202 (2019).
[55]M. Barone, C. Du, L. Radosavljevic, D. Werder, X. Pan, and D. G. Schlom, "Epitaxial synthesis of a vertically aligned two-dimensional van der Waals crystal: (110)-oriented SnO," Cryst. Growth Des. **22**(12), 7248–7254 (2022).
[56]K. M. Adkison, S. L. Shang, B. J. Bocklund, D. Klimm, D. G. Schlom, and Z. K. Liu, "Suitability of binary oxides for molecular-beam epitaxy source materials: A comprehensive thermodynamic analysis," APL Mater. **8**(8), 081110 (2020).
[57]H. Paik, Z. Chen, E. Lochocki, H. Ariel Seidner, A. Verma, N. Tanen, J. Park, M. Uchida, S. Shang, B. C. Zhou, M. Brützam, R. Uecker, Z. K. Liu, D. Jena, K. M. Shen, D. A. Muller, and D. G. Schlom, "Adsorption-controlled growth of La-doped $BaSnO_3$ by molecular-beam epitaxy," APL Mater. **5**(11), 116107 (2017).
[58]G. Hoffmann, M. Budde, P. Mazzolini, and O. Bierwagen, "Efficient suboxide sources in oxide molecular beam epitaxy using mixed metal + oxide charges: The examples of SnO and Ga_2O," APL Mater. **8**(3), 031110 (2020).
[59]P. Vogt, F. V. E. Hensling, K. Azizie, C. S. Chang, D. Turner, J. Park, J. P. McCandless, H. Paik, B. J. Bocklund, G. Hoffman, O. Bierwagen, D. Jena, H. G. Xing, S. Mou, D. A. Muller, S. L. Shang, Z. K. Liu, and D. G. Schlom, "Adsorption-controlled growth of $Ga_2O_3$by suboxide molecular-beam epitaxy," APL Mater. **9**(3), 031101 (2021).
[60]P. Vogt, D. Schlom, F. Hensling, K. Azizie, Z.-K. Liu, B. Bocklund, and S.-L. Shang, "Suboxide molecular-beam epitaxy and related structures," U.S. patent 11,462,402 (October 4, 2022).
[61]S. Hishita, P. Janeček, and H. Haneda, "Epitaxial growth of tin oxide film on TiO_2(1 1 0) using molecular beam epitaxy," J. Cryst. Growth **312**(20), 3046–3049 (2010).
[62]A. Nikiforov, V. Timofeev, V. Mashanov, I. Azarov, I. Loshkarev, V. Volodin, D. Gulyaev, I. Chetyrin, and I. Korolkov, "Formation of SnO and SnO_2 phases during the annealing of SnO(x) films obtained by molecular beam epitaxy," Appl. Surf. Sci. **512**, 145735 (2020).
[63]M. Budde, P. Mazzolini, J. Feldl, C. Golz, T. Nagata, S. Ueda, G. Hoffmann, F. Hatami, W. T. Masselink, M. Ramsteiner, and O. Bierwagen, "Plasma-assisted molecular beam epitaxy of SnO(001) films: Metastability, hole transport properties, Seebeck coefficient, and effective hole mass," Phys. Rev. Mater. **4**(12), 124602 (2020).
[64]T. A. Kraay, J. R. Kim, J. Falson, S.-L. Shang, Z.-K. Liu, and D. G. Schlom, "Surface preparation of oxide substrates by *in situ* laser annealing" (unpublished).
[65]T. Schwaigert, S. Salmani-Rezaie, M. R. Barone, H. Paik, E. Ray, M. D. Williams, D. A. Muller, D. G. Schlom, and K. Ahadi, "Molecular beam epitaxy of $KTaO_3$," J. Vac. Sci. Technol. A **41**, 022703 (2023).
[66]L. J. van der Pauw, "A method of measuring specific resistivity and Hall effect of discs of arbitrary shape," Philips Res. Rep. **13**, 1–9 (1958).
[67]J. A. Woollam, B. D. Johs, C. M. Herzinger, J. N. Hilfiker, R. A. Synowicki, and C. L. Bungay, "Overview of variable-angle spectroscopic ellipsometry (VASE): I. Basic theory and typical applications," Proc. SPIE **10294**, 1029402 (1999).
[68]J. Lee, P. I. Rovira, I. An, and R. W. Collins, "Rotating-compensator multichannel ellipsometry: Applications for real time Stokes vector spectroscopy of thin film growth," Rev. Sci. Instrum. **69**(4), 1800–1810 (1998).
[69]E. Amonette, P. Dulal, D. Sotir, M. Barone, D. Schlom, and N. J. Podraza, "Band gap energy and near infrared to ultraviolet complex optical properties of single crystal $TbScO_3$," Appl. Phys. Lett. **123**, 052103 (2023).

[70]L. Karki Gautam, H. Haneef, M. M. Junda, D. B. Saint John, and N. J. Podraza, "Approach for extracting complex dielectric function spectra in weakly-absorbing regions," Thin Solid Films **571**, 548–553 (2014).
[71]H. F. Haneef and N. J. Podraza, "Optical properties of single crystal $Bi_4Ge_3O_{12}$ from the infrared to ultraviolet," J. Appl. Phys. **116**, 163507 (2014).
[72]K. Ghimire, H. F. Haneef, R. W. Collins, and N. J. Podraza, "Optical properties of single-crystal $Gd_3Ga_5O_{12}$ from the infrared to ultraviolet," Phys. Status Solidi B **252**(10), 2191–2198 (2015).
[73]S. Stoughton, M. Showak, Q. Mao, P. Koirala, D. A. Hillsberry, S. Sallis, L. F. Kourkoutis, K. Nguyen, L. F. J. Piper, D. A. Tenne, N. J. Podraza, D. A. Muller, C. Adamo, and D. G. Schlom, "Adsorption-controlled growth of $BiVO_4$ by molecular-beam epitaxy," APL Mater. **1**(4), 042112 (2013).
[74]E. Amonette, P. Dulal, M. Mainali, and N. J. Podraza, "Optical properties of yttria-stabilized zirconia from spectroscopic ellipsometry," Surf. Sci. Spectra **31**(1), 016001 (2024).
[75]H. Fujiwara, J. Koh, P. I. Rovira, and R. W. Collins, "Assessment of effective-medium theories in the analysis of nucleation and microscopic surface roughness evolution for semiconductor thin films," Phys. Rev. B **61**(16), 10832–10844 (2000).
[76]R. W. Collins and A. S. Ferlauto, *Handbook of Ellipsometry* (Williams Andrew, Norwich, NY, 2005).
[77]G. E. Jellison, N. J. Podraza, and A. Shan, "Ellipsometry: Dielectric functions of anisotropic crystals and symmetry," J. Opt. Soc. Am. A **39**(12), 2225–2237 (2022).
[78]W. G. Oldham, "Numerical techniques for the analysis of lossy films," Surf. Sci. **16**, 97–103 (1969).
[79]F. C. Frank, "The influence of dislocations on crystal growth," Discuss. Faraday Soc. **5**, 48–79 (1949).
[80]F. C. Frank, "Crystal growth and dislocations," Adv. Phys. **1**(1), 91–109 (1952).
[81]J. C. Fisher, R. L. Fullman, and G. W. Sears, "On the origin of screw dislocations in growing crystals," Acta Metall. **2**, 344–346 (1954).
[82]G. G. Lemmlein and E. D. Dukova, "Formation of screw dislocations in the growth process of a crystal," Sov. Phys. Crystallogr. **1**, 269–273 (1956).
[83]M. I. Kozlovskii, "Formation of screw dislocations in the growth of a crystal around solid particles," Sov. Phys. Crystallogr. **3**, 205–211 (1958).
[84]M. I. Kozlovskii, "Formation of screw dislocations at the junction of two layers spreading over the surface of a crystal," Sov. Phys. Crystallogr. **3**, 205–211 (1958).
[85]A. Baronnet, "Sur les origines des dislocations vis et des spirales de croissance dans les micas," J. Cryst. Growth **19**(3), 193–198 (1973).
[86]D. G. Schlom, D. Anselmetti, J. G. Bednorz, Ch. Gerber, and J. Mannhart, "Epitaxial growth of cuprate supersonductors from the gas phase," J. Cryst. Growth **137**(1-2), 259–267 (1994).
[87]G. W. Brown, M. E. Hawley, C. D. Theis, J. Yeh, and D. G. Schlom, "Atomic force microscopy examination of the evolution of the surface morphology of $Bi_4Ti_3O_{12}$ grown by molecular beam epitaxy," J. Electroceram. **4**, 351–356 (2000).
[88]J. Lettieri, Y. Jia, S. J. Fulk, D. G. Schlom, M. E. Hawley, and G. W. Brown, "Optimization of the growth of epitaxial $SrBi_2Ta_2O_9$ thin films by pulsed laser deposition," Thin Solid Films **379**, 64–71 (2000).
[89]J. B. Nelson and D. P. Riley, "An experimental investigation of extrapolation methods in the dimensions of crystals derivation of accurate unit-cell," Proc. Phys. Soc. **57**, 160 (1945).
[90]J. L. Lyons, A. Janotti, and C. G. Van de Walle, "Shallow versus deep nature of Mg acceptors in nitride semiconductors," Phys. Rev. Lett. **108**(15), 156403 (2012).
[91]J. Neugebauer and C. G. Van de Walle, "Chemical trends for acceptor impurities in GaN," J. Appl. Phys. **85**(5), 3003–3005 (1999).
[92]V. Fiorentini, F. Bernardini, A. Bosin, and D. Vanderbilt, "*Ab initio* shallow acceptor levels in gallium nitride," in *Proceedings of the 23rd International Conference on the Physics of Semiconductors*, edited by M. Scheffler and R. Zimmermann (World Scientific, Singapore, 1996), p. 2877.
[93]S. Brochen, J. Brault, S. Chenot, A. Dussaigne, M. Leroux, and B. Damilano, "Dependence of the Mg-related acceptor ionization energy with the acceptor concentration in p-type GaN layers grown by molecular beam epitaxy," Appl. Phys. Lett. **103**(3), 032102 (2013).
[94]H. Nakayama, P. Hacke, M. R. H. Khan, T. Detchprohm, K. H. Kazumasa Hiramatsu, and N. S. Nobuhiko Sawaki, "Electrical transport properties of p-GaN," Jpn. J. Appl. Phys. **35**(3A), L282 (1996).
[95]M. Ilegems, R. Dingle, and R. A. Logan, "Luminescence of Zn- and Cd-doped GaN," J. Appl. Phys. **43**(9), 3797–3800 (1972).
[96]B. Monemar, H. P. Gislason, and O. Lagerstedt, "Properties of Zn-doped VPE-grown GaN. II. Optical cross sections," J. Appl. Phys. **51**(1), 640–649 (1980).
[97]N. F. Quackenbush, J. P. Allen, D. O. Scanlon, S. Sallis, J. A. Hewlett, A. S. Nandur, B. Chen, K. E. Smith, C. Weiland, D. A. Fischer, J. C. Woicik, B. E. White, G. W. Watson, and L. F. J. Piper, "Origin of the bipolar doping behavior of SnO from X-ray spectroscopy and density functional theory," Chem. Mater. **25**(15), 3114–3123 (2013).

Supplementary Information

Controlling the p-type conductivity of α-SnO thin films by potassium doping

Sieun Chae,[1,§] Seungmin Lee,[1,§] Anna Park,[1,§] M. K. Indika Senevirathna,[2,§] Yufan Feng,[3] Venkanna Kanneboina,[4,5] Viet-Anh Ha,[6,7] Yaoqiao Hu,[8] Chaojie Du,[9] Matthew Barone,[10] Vladimir Protasenko,[11] Yilin Evan Li[1], Nikolas Podraza,[4,5] Kedar Johnson,[2] Debdeep Jena,[1,11,12] Huili G. Xing,[1,11,12] Xiaoqing Pan,[9] Kyeongjae Cho,[8] Feliciano Giustino,[6] Michael D. Williams,[2] and Darrell G. Schlom[1,10,12,13*]

[1]Department of Materials Science and Engineering, Cornell University, Ithaca, NY 14853, United States
[2]Department of Physics, Clark Atlanta University, GA 30314, United States
[3]Robert Frederick Smith School of Chemical and Biomolecular Engineering, Cornell University, Ithaca, NY 14853, United States
[4]Department of Physics and Astronomy, The University of Toledo, OH 43606, United States
[5]Wright Center for Photovoltaics Innovation and Commercialization, The University of Toledo, OH 43606, United States
[6]Oden Institute for Computational Engineering and Sciences, The University of Texas at Austin, Austin, TX 78712, United States
[7]Department of Physics, The University of Texas at Austin, Austin, TX 78712, United States
[8]Department of Materials Science and Engineering, University of Texas at Dallas, TX 75080, United States
[9]Department of Materials Science and Engineering, University of California at Irvine, Irvine, CA 92697, United States
[10]Platform for the Accelerated Realization, Analysis, and Discovery of Interface Materials (PARADIM), Cornell University, Ithaca, NY 14853, United States
[11]School of Electrical and Computer Engineering, Cornell University, Ithaca, NY 14853, United States
[12]Kavli Institute at Cornell for Nanoscale Science, Ithaca, NY 14853, United States
[13]Leibniz-Institut fur Kristallzüchtung, 12489 Berlin, Germany

*Correspondence to: schlom@cornell.edu
[§]These authors contributed equally

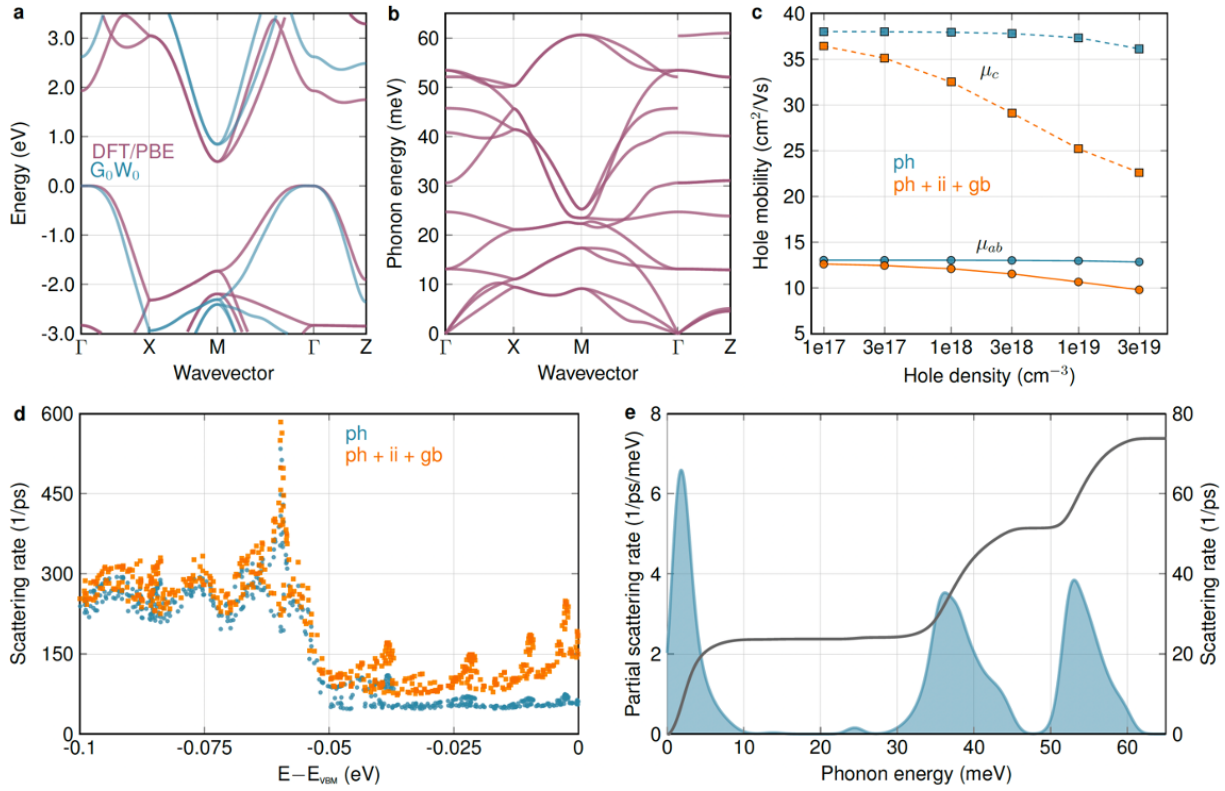

Figure S1. (a) DFT and *GW* band structures. (b) Phonon band structure. (c) Hole mobility at room-temperature as a function of hole density. Phonon-limited mobility is obtained with *GW* band structure and quadrupole long-range electron-phonon interaction (cyan). Extrinsic scattering mechanisms such as ionized-impurity and grain boundary are also considered (orange). The hole mobilities in the *ab*-plane and along the *c*-axis of tetragonal SnO are indicated by solid and dashed lines, respectively. (d) Hole scattering rate at a doping of 10^{18} cm^{-3} in the energy range of 100 meV with reference to the valence band maximum (VBM). (e) Partial scattering rates of holes by phonons in SnO, resolved by phonon mode energy (cyan line and filled area). The gray line is the cumulative scattering rate, i.e., the running integral of the blue curve, as reported on the right axis.

Table S1. Calculated dynamical quadrupole tensors for SnO, in units of e·bohr. Calculations performed using the DFPT framework of Ref. 1, as implemented in the Abinit code.[2]

Atom	Cart. Dir.	$\boldsymbol{Q_{xx}}$	$\boldsymbol{Q_{yy}}$	$\boldsymbol{Q_{zz}}$	$\boldsymbol{Q_{yz}}$	$\boldsymbol{Q_{xz}}$	$\boldsymbol{Q_{xy}}$
Sn-1	*x*	0.00000	0.00000	0.00000	0.00000	-2.32313	0.00000
	y	0.00000	0.00000	0.00000	-2.32313	0.00000	0.00000
	z	0.17158	0.17158	-0.57381	0.00000	0.00000	0.00000
Sn-2	*x*	0.00000	0.00000	0.00000	0.00000	2.32313	0.00000
	y	0.00000	0.00000	0.00000	2.32313	0.00000	0.00000
	z	-0.17158	-0.17158	0.57381	0.00000	0.00000	0.00000
O-1	*x*	0.00000	0.00000	0.00000	0.00000	-9.74132	0.00000
	y	0.00000	0.00000	0.00000	9.74132	0.00000	0.00000
	z	-10.72717	10.72717	0.00000	0.00000	0.00000	0.00000
O-2	*x*	0.00000	0.00000	0.00000	0.00000	9.74132	0.00000
	y	0.00000	0.00000	0.00000	-9.74132	0.00000	0.00000
	z	10.72717	-10.72717	0.00000	0.00000	0.00000	0.00000

Table S2. The substrate temperature (T_{sub}) and potassium effusion cell temperature ($T_{K\ effusion\ cell}$) of the samples presented in this work.

	T_{sub}	$T_{K\ effusion\ cell}$
A1	375 °C	260 °C
A2	375 °C	250 °C
A3	375 °C	240 °C
A4	375 °C	220 °C
A5	375 °C	200 °C
A6	300 °C	160 °C
A7	330 °C	200 °C
A8	285 °C	200 °C
A9	300 °C	207 °C
A10	285 °C	210 °C
A11	330 °C	220 °C
A12	330 °C	235 °C
A13	285 °C	250 °C
A14	330 °C	27 °C
A15	330 °C	27 °C
A16	270 °C	27 °C
A17	300 °C	27 °C
A18	320 °C	27 °C
A19	375 °C	27 °C
A20	320 °C	27 °C
A21	320 °C	27 °C

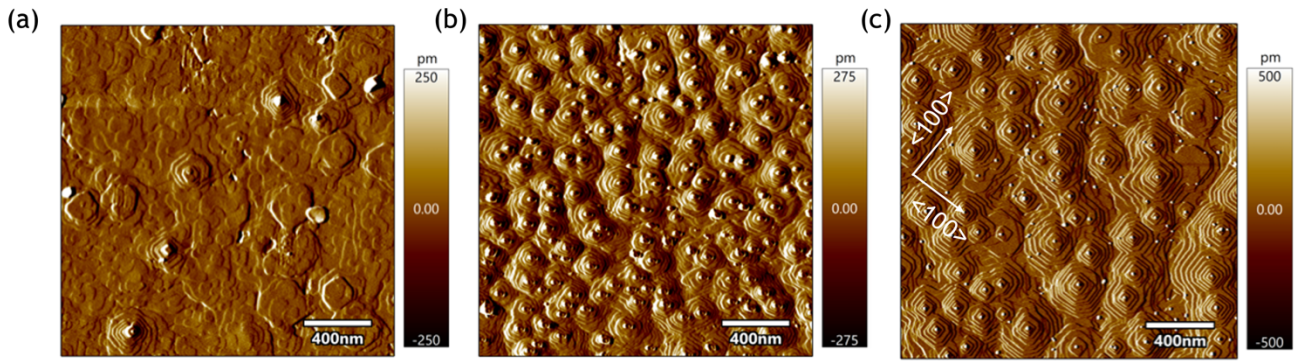

Figure S2. Atomic force microscopy of (a) Sample A21—an undoped α-SnO thin film grown at low SnO flux (2×10^{12} molecules/(cm^2 s)), (b) Sample A20—an undoped α-SnO thin film grown at high SnO flux (1×10^{13} molecules/(cm^2 s)), (c) Sample A18—a K-doped α-SnO thin film grown at low SnO flux (2×10^{12} molecules/(cm^2 s)) on a YSZ (001) substrate. The in-plane <100> directions of α-SnO are indicated. The films contain growth spirals with densities ranging from (a) 1.3×10^{8} cm^{-2} to (b) 3.1×10^{9} cm^{-2} to (c) 1.5×10^{9} cm^{-2}. The diameter of the grain ranges from 100 nm to 200 nm.

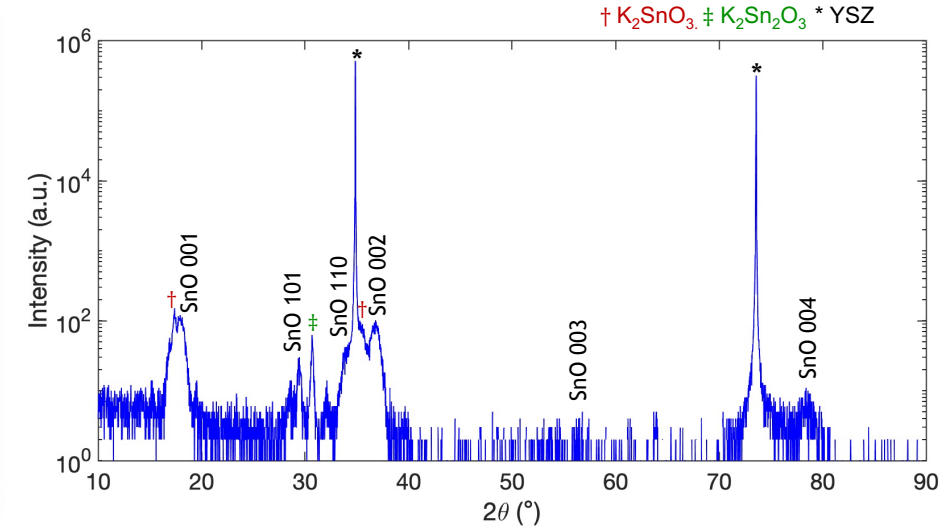

Fig. S3. θ-2θ X-ray diffraction scan of K-doped α-SnO thin film grown on YSZ (100) substrate with $T_{\text{K effusion cell}}$ = 280 °C and possible phases that could give rise to the peak positions observed.

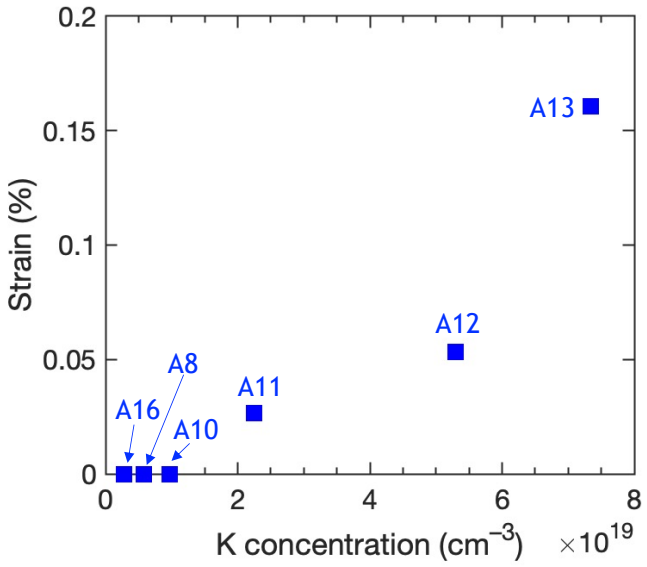

Figure S4. The out-of-plane strain of K-doped SnO thin films with varied K concentration.

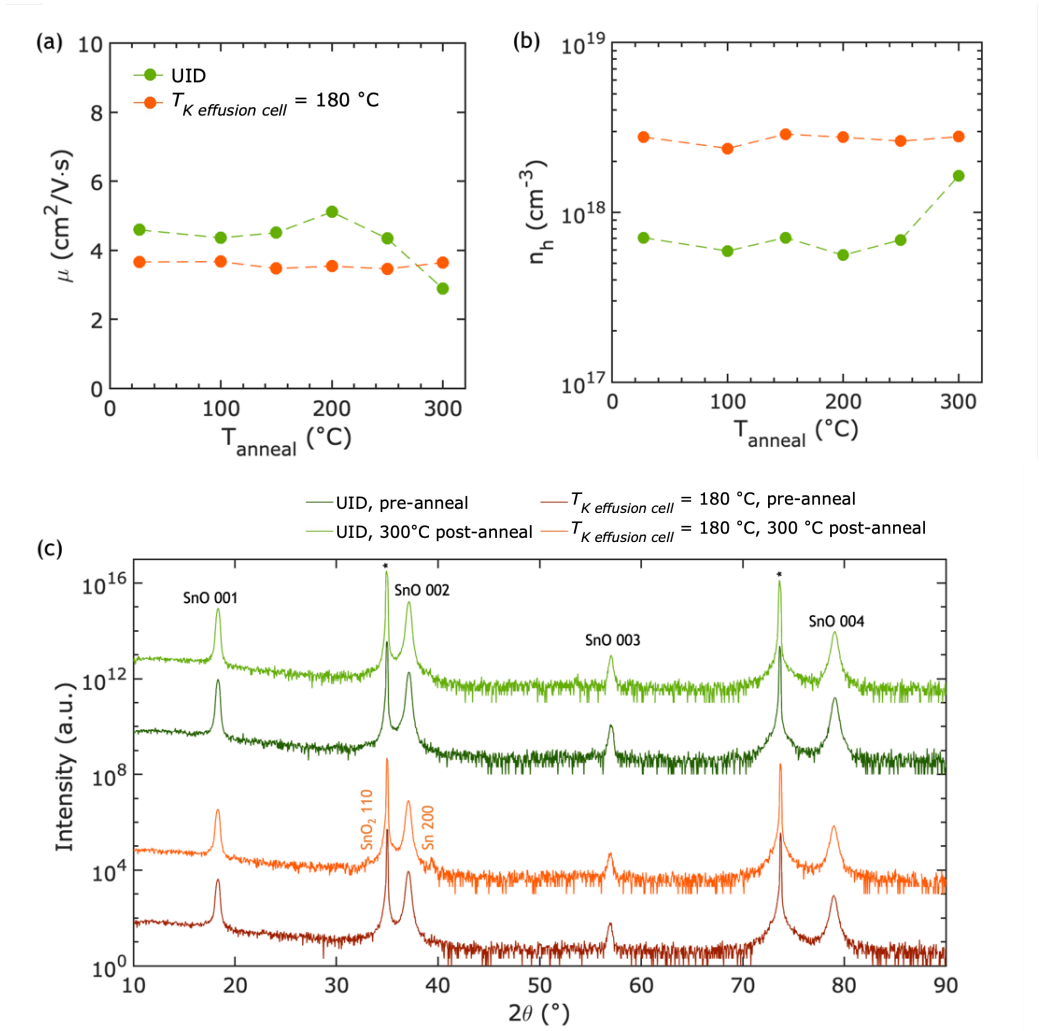

Figure S5. Thermal stability of undoped α-SnO (UID) and K-doped α-SnO ($T_{\text{K effusion cell}}$ = 180 °C). (a-b) The measured (a) Hall mobility and (b) hole carrier concentration of undoped α-SnO and K-doped α-SnO thin films as a function of post annealing temperature. The Hall measurement is performed at room temperature after cooling down the post-annealed samples. (c) X-ray diffraction pattern of undoped α-SnO and K-doped α-SnO thin films before and after annealing at 300 °C. The start of phase decomposition is observed for the post-annealed K-doped α-SnO thin films.

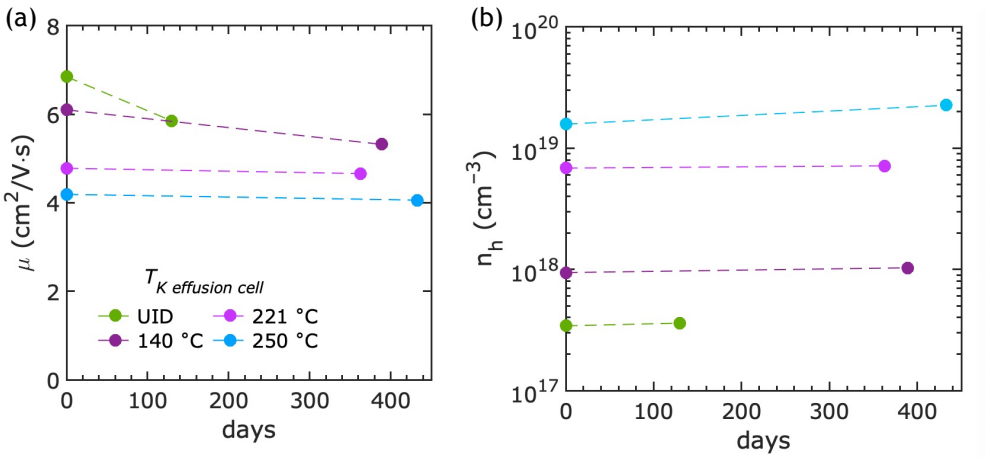

Figure S6. Time stability of undoped α-SnO (UID) and K-doped α-SnO with varied $T_{K\ effusion\ cell}$. (a) Hall mobility and (b) hole carrier concentration are measured as a function of the days after deposition.

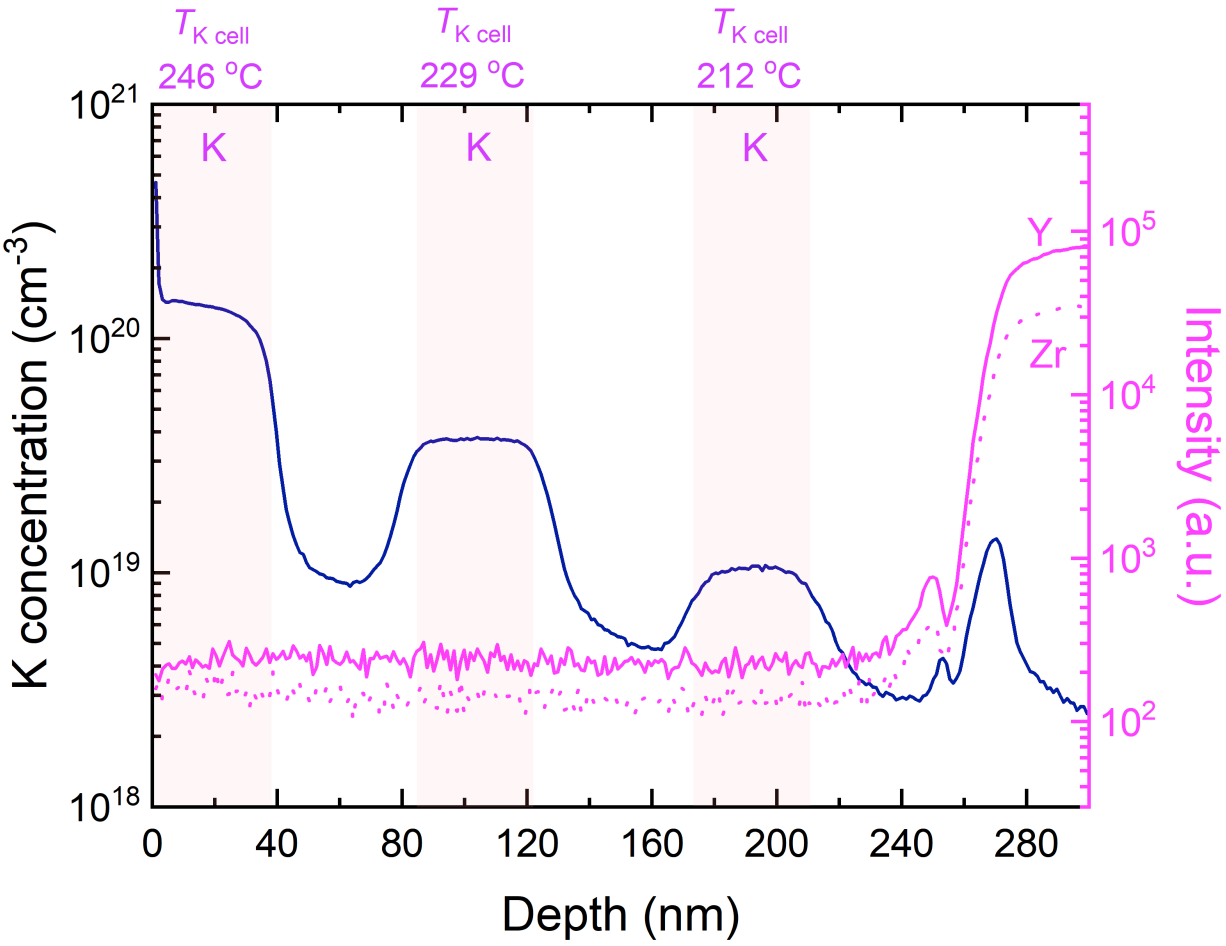

Figure S7. A depth profile showing the potassium concentration measured by SIMS for a multilayer consisting of alternating K-doped α-SnO and undoped α-SnO layers. The potassium effusion cell temperature is varied for the three K-doped α-SnO layers. The sharp increase in the SIMS intensity from yttrium and zirconium denotes the location of the interface with the underlying YSZ substrate.

Table S3. Layer thicknesses and optical property parameters for epitaxial α-SnO films (Samples A5, A4, A3, and A2) with varied potassium concentration controlled by $T_{K\ effusion\ cell}$ obtained with divided spectral range analysis. Here the parameters A_n, Γ_n, E_n, ϕ_n, and μ_n are the amplitude, broadening, transition energy, phase projector factor, and dimensionality factor from the critical point parabolic band (CPPB) oscillator model, respectively, and A_s and E_s are the amplitude and resonance energy of the Sellmeier expression, respectively.

Model parameters	Undoped SnO	K-doped SnO ($T_{K\ effusion\ cell}$ = 200 °C)	K-doped SnO ($T_{K\ effusion\ cell}$ = 220 °C)	K-doped SnO ($T_{K\ effusion\ cell}$ = 240 °C)	K-doped SnO ($T_{K\ effusion\ cell}$ = 250 °C)
Transparent region					
Sellmeier A_s(eV^2)	136 ± 2	135 ± 3	133 ± 5	132 ± 5	118 ± 1
Sellmeier E_s (eV)	4.52 ± 0.03	4.52 ± 0.04	4.46 ± 0.07	4.46 ± 0.07	4.30 ± 0.01
Highly absorption region					
Sellmeier A_s (eV^2)	222 ± 15	229 ± 17	0	0	240 ± 17
Sellmeier E_s (eV)	8.5 ± 0.2	8.7 ± 0.3	11	11	8.5 ± 0.3
A_1 (unitless)	4.5 ± 0.4	5.8 ± 0.6	4.6 ± 0.6	5.0 ± 0.5	7.3 ± 0.4
Γ_1 (eV)	0.38 ± 0.02	0.44 ± 0.02	0.44 ± 0.04	0.4 ± 0.3	0.55 ± 0.02
En_1 (eV)	3.12 ± 0.01	3.13 ± 0.01	3.10 ± 0.02	3.10 ± 0.02	3.100 ± 0.009
ϕ_1 (deg)	21 ± 7	13.5 ± 6.8	360 ± 11	360 ± 12	344 ± 5
μ_1	1	1	1	1	1
A_2 (unitless)	22.3 ± 0.4	21.4 ± 0.5	19.4 ± 0.9	19.1 ± 1.1	15.5 ± 0.4
Γ_2 (eV)	0.670 ± 0.009	0.65 ± 0.01	0.67 ± 0.02	0.67 ± 0.01	0.71 ± 0.01
En_2 (eV)	3.480 ± 0.005	3.480 ± 0.005	3.530 ± 0.008	3.530 ± 0.008	3.510 ± 0.006
ϕ_2 (deg)	-46 ± 1	-49 ± 2	-35 ± 3	-37 ± 3	-50 ± 2
μ_2	1	1	1	1	1
A_3 (unitless)	8 ± 1	7.4 ± 0.9	5.2 ± 0.2	5.1 ± 0.2	9.2 ± 2.1
Γ_3 (eV)	1.7 ± 0.1	1.8 ± 0.1	4.4 ± 0.2	4.5 ± 0.2	1.6 ± 0.2
En_3 (eV)	6.35 ± 0.07	6.36 ± 0.08	4.5 ± 0.1	4.5 ± 0.1	6.6 ± 0.1
ϕ_3 (deg)	89 ± 7	87 ± 8	-47 ± 2	-47 ± 2	103 ± 10
μ_3	1	1	1	1	1
Surface roughness thickness (nm)	5.97 ± 0.08	5.4 ± 0.2	5.1 ± 0.3	5.8 ± 0.4	5.08 ± 0.07
Bulk thickness (nm)	55 ± 1	56 ± 1	52 ± 2	52 ± 2	56 ± 1
Interface thickness (nm)	19.6 ± 0.5	17 ± 1	17.2 ± 1.9	15.4 ± 2.1	0
Interface void fraction (%)	24.7 ± 1.9	25.7 ± 3.2	26 ± 6	25.5 ± 6.6	0

References

[1] M. Royo and M. Stengel, Phys. Rev. X **9**, 021050 (2019).

[2] X. Gonze, B. Amadon, G. Antonius, F. Arnardi, L. Baguet, J.M. Beuken, J. Bieder, F. Bottin, J. Bouchet, E. Bousquet, N. Brouwer, F. Bruneval, G. Brunin, T. Cavignac, J.B. Charraud, W. Chen, M. Côté, S. Cottenier, J. Denier, G. Geneste, P. Ghosez, M. Giantomassi, Y. Gillet, O. Gingras, D.R. Hamann, G. Hautier, X. He, N. Helbig, N. Holzwarth, Y. Jia, F. Jollet, W. Lafargue-Dit-Hauret, K. Lejaeghere, M.A.L. Marques, A. Martin, C. Martins, H.P.C. Miranda, F. Naccarato, K. Persson, G. Petretto, V. Planes, Y. Pouillon, S. Prokhorenko, F. Ricci, G.M. Rignanese, A.H. Romero, M.M. Schmitt, M. Torrent, M.J. van Setten, B. Van Troeye, M.J. Verstraete, G. Zérah, and J.W. Zwanziger, Comput. Phys. Commun. **248**, 107042 (2020).